PHYSICAL REVIEW B VOLUME 32, NUMBER 6 15 SEPTEMBER 1985

Polytope model and the electronic and structural properties of amorphous semiconductors

R. Mosseri
Laboratoire de Physique des Solides, Centre National de la Recherche Scientifique, F-92195 Meudon (Principal Cédex), France

D. P. DiVincenzo
Laboratory of Atomic and Solid State Physics and Materials Science Center, Cornell University, Ithaca, New York 14853

J. F. Sadoc
Laboratoire de Physique des Solides, Centre National de la Recherche Scientifique, Université de Paris—Sud, F-91405 Orsay (Cédex), France

M. H. Brodsky
IBM Thomas J. Watson Research Center, Yorktown Heights, New York 10598
(Received 12 April 1985)

A model for describing a new kind of order in amorphous covalently-bonded networks is described. We introduce the concept of "propagated short-range order" (SRO), which expresses the idea that SRO about a particular atom can constrain the form of SRO around neighboring atoms. Propagated SRO can be achieved by applying a certain network-building rule to every site in the solid. For example, the rule "Place eight cubes around each vertex" generates a simple-cubic crystal. However, some ways of propagating SRO are incompatible with long-range crystalline order; specific examples of this frustrated propagation are shown in two and three dimensions. Many interesting kinds of propagated short-range order are compatible with translationally ordered structures called polytopes, which are large molecules or crystals in non-Euclidean space. We propose that certain types of polytope order describe intermediate-range order in amorphous semiconductors. Therefore, the quantum numbers labeling the symmetries of these polytopes provide approximate symmetry labels for electronic eigenstates of the amorphous solid. We explain the symmetry groups of the polytopes in detail; these are discrete subgroups of SO(4). We use their irreducible representations to construct the analogy of the energy-band dispersion for the amorphous solid. If patches of polytope order exist in the amorphous solid, then an approximate vertical selection rule should govern optical absorption in these materials, and we suggest it as part of a possible explanation of the depressed optical absorption near the band edge in hydrogenated amorphous silicon.

I. INTRODUCTION

It is well known that there exist substantial similarities between the electronic properties of crystalline and amorphous semiconductors.[1] Both have an occupied valence band of about the same width and with generally the same peak structure, and both have a forbidden energy gap of about the same size. The similarities become even more pronounced when the amorphous semiconductor is prepared in such a way that most of the chemical bonds are satisfied; this can be accomplished by growth at higher temperatures or by the incorporation of impurity atoms (e.g., H or F). In these materials the density of states in the energy gap is very small and the electrical properties can be changed by acceptor or donor doping just as in the crystal.[2] It is the purpose of this paper to explore some of the possible causes of this similarity.

Of course, it is well known that the short-range order (SRO) is essentially the same in the connected amorphous network and in the crystalline network; in both crystalline and amorphous group-IV semiconductors, each atom forms four covalent bonds with its nearest neighbors. It is quite reasonable to attribute much of the similarity in the electronic structure to this SRO. However, we will assert that there is a deeper similarity between the amorphous and crystalline systems, and that the amorphous network has a greater degree of order than just SRO. The presence of SRO at one point in a lattice forces a similar kind of SRO at neighboring points. We will make this concept more concrete later, but for the time being a simple example will suffice: If the four sp_3 bonds are oriented at a particular direction at one lattice site, then the orientation of the tetrahedral bonds on neighboring atoms is at least partially determined. This is the the most elementary manifestation of what we call *propagated SRO*. There are thus two distinct features of SRO which should be remembered: (a) There are physical and chemical reasons why the SRO occurring on neighboring sites is correlated; (2) therefore, SRO has a tendency to propagate in a particular way over long distances in the network. This propagation may or may not be geometrically allowed.

In the crystalline network the SRO is the same everywhere; we say that in this case SRO propagates *rigidly* in all directions, leading to perfect translational order. We will show that there exist forms of SRO ("polytope order")[3,4] which are natural to the tetrahedrally-bonded net-

work but whose rigid propagation throughout all space is impossible. This will be suggested as a possible reason for the long-range disorder in the amorphous solid. However, this order can propagate over some intermediate distance in the network, and an approximate translational symmetry can be associated with this propagation.[5] This translational symmetry can be used in the same way as in the crystalline state: a Bloch theorem for eigenstates can be shown, and symmetry selection rules for optical absorption can be derived. This will be done in the present paper. Thus we hope to show that the amorphous and crystalline networks have more in common than was previously supposed, and that the similarities in the properties mentioned above are quite understandable.

To begin, we must be more precise about the nature of SRO in a group-IV semiconductor network.[6,7] The most basic property of such a network is its fourfold coordination. The primitive element of SRO might then be chosen to be the tetrahedron of orbitals surrounding each atom. Instead, we have chosen our fundamental local structural unit to be the six-membered ring of bonds. This is reasonable, since many of the crystalline modifications of Si and Ge contain only six-membered rings, and numerical simulations of random networks show a majority of six-membered rings, although five- and seven-membered rings do occur. In the diamond crystal structure, the "*chair-type*" six-membered ring is propagated uniformly throughout all space. In wurtzite (or lonsdaleite) a combination of chair-type and "*boat-type*" rings constitute the fundamental unit of SRO. These two modifications of six-membered rings are shown in Fig. 1. They merely represent two different ways of constructing a ring of six equal-length bonds with tetrahedral angles ($\approx 109°$) at the joints. Since the optimal bond angles and bond lengths occur in these structures, they should be of particularly low energy. However, they are not the only six-fold rings which satisfy these constraints. Figure 1 shows a third ring, of a "*twisted boat* type," which is distinct from the other two and which has ideal bond angles and bond lengths as well. (In fact, there is a continuous family of boat-type six-membered rings which satisfy all bond-length and bond-angle constraints.[8]) The twisted boat ring of Fig. 1(c) is distinguished by the three mutually-perpendicular twofold symmetry axes passing through its center. Rings of approximately this geometry have been found to occur in numerically generated random network models for group-IV semiconductors;[8–10] thus it seems that we must include the twisted boat as a possible fundamental local structure unit as well.

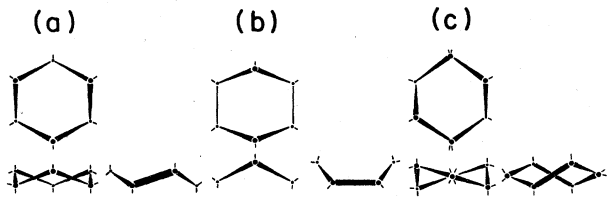

FIG. 1. Top, front, and side views of six-membered rings. (a) The "chair." (b) The "boat." (c) The "twisted boat," a new type.

How can the SRO represented by the twisted boat propagate? It has already been shown that three twisted boats can be joined together to form the structure in Fig. 2, which has been called the "little barrel" ("*petit barrelan*"[7]). A natural way of propagating this SRO is given by the rule "Insert the tips of four barrels around each atom." The resulting structure in the vicinity of one atom is shown in Fig. 3. After the building rule has been applied to several atoms, the "*petit barrelan*" will become twisted, as the figure shows. Both the "*petit barrelan*" itself and the structure of Fig. 3 have also been seen in numerical network simulations.[9] The 27-atom cluster of Fig. 3 has a very interesting property which makes it likely to occur: The number of dangling bonds pointing outward from this cluster (28) is smaller than the number of dangling bonds in any comparable-size cluster with diamondlike or wurtzitelike structure (i.e., with boat and chair rings).[11] Thus the propagated SRO resulting from the twisted boat ring may give lower-energy configurations for small numbers of atoms than propagated boat- or chair-ring order. The natural next step is to try to extend the SRO in Fig. 3 to larger structures, i.e., to apply the rule "four '*petits barrelans*' around each vertex" to successive atoms in the system, but it does not work. Departures from perfect bond angles and bond lengths become larger and larger as the rule is applied further and further from the center of Fig. 3. By the time 50 or so atoms have been added, the rule leads to unrealistically distorted structures, and defects must begin to appear.

We see that the propagation of a very natural kind of SRO (as represented, for example, by the twisted boat ring or the "*petit barrelan*") need not lead to crystalline long-range order. This type of SRO still may be very important for the disordered network, since it may describe favorable structures of intermediate size. We will show that we can generalize the concept of "crystal" to naturally describe the ideal state of perfectly-propagated SRO of this type. It will be the quantum numbers labeling the approximate symmetries of this generalized crystal which will permit us to make analogies between the disordered and crystalline networks.

The remainder of this paper is organized as follows. In Sec. II some general concepts of propagated SRO are in-

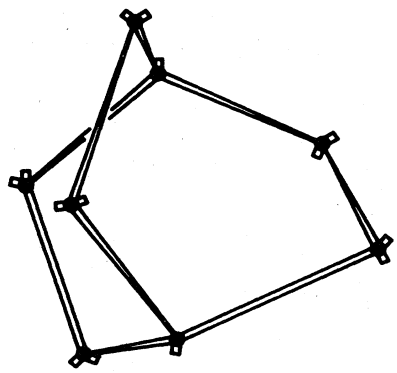

FIG. 2. The "little barrel" (*"petit barrelan"*). In the polytope model, this is a possible fundamental unit of short-range order.

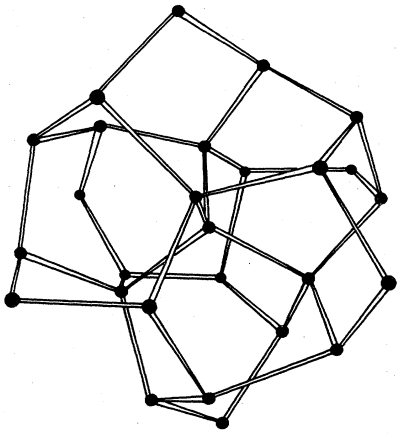

FIG. 3. An assembly of four "*petits barrelans*" around a central atom forming a 27-atom cluster. It is the smallest cluster in which all six-membered rings are complete around the central atom. This cluster has fewer dangling bonds than a diamond-like cluster of the same type.

troduced. We will use an example in two dimensions to illustrate a SRO which does not lead to a crystal, introduce the notion of a polytope as a natural generalization of a crystal, and show how polytope symmetries are related to approximate symmetries in the real disordered network. In Sec. III we outline the formal theory of the symmetry of polytopes which are representative of structure in three-dimensional covalent networks. We present the concept of an energy-band structure for the polytopes in Sec. IV. In Sec. V we work out a more detailed and realistic electronic structure for one particular polytope which seems most representative of order in amorphous semiconductors; in Sec. VI a model optical-absorption calculation based on this band structure is presented. We present our conclusions in Sec. VII. There are two appendixes; in Appendix A some details of the mathematical treatment of quaternions are given, and in Appendix B the effect of disclinations on the electronic spectrum of the polytopes is discussed.

II. GENERAL CONCEPTS

In this section we show how polytope lattice structures are naturally related to various rules for propagated SRO, how the polytope electronic structure can be computed, how it can be related approximately to the local electronic structure of a disordered network, and how the symmetries of the polytope are related to approximate local symmetries in the disordered system. Polytopes[12] may be defined as crystals in non-Euclidean space, or as Platonic solids in higher dimensions. We will illustrate the polytope concept using a two-dimensional example. It is vastly more easy to visualize and draw lattices in two dimensions than in three, and almost all of the ideas we present here will be simply generalizable later to one higher dimension.

Consider a structure in which the fundamental local unit of SRO is a five-membered ring or pentagon.[13] We might imagine a system in which the fundamental rule for the propagation of SRO is "join three pentagons together at every vertex." This rule clearly does not fill the two-dimensional plane; as Fig. 4 shows, this propagation suffers the same problem as the fitting together of "*petits barrelans*" mentioned above. The structure is sensible locally, but very quickly leads to unreasonably large distortions. In order to complete the tiling of the plane, violations of the propagation rule must be introduced (e.g., four pentagons meeting at a point). The crucial observation made some years ago by one of us[3,4] is that there *is* a sort of crystal which corresponds to the rigid propagation of this SRO as well as many others; it is, however, a crystal lying on a curved, non-Euclidean space, which has been called a *polytope*. The three-pentagons-per-vertex rule works perfectly in two-dimensional (2D) space with a particular positive curvature, and the resulting structure is the dodecahedron [Fig. 5(a)]. The dodecahedron is an example of a polytope in 2D space, which is also called a polyhedron. Its structure may be representative of a piece of a disordered lattice in two dimensions [see the right-hand side of Fig. 5(a)], and a mapping may be devised from one to the other, as suggested by the vertex numbering in the figure. The degree of local disorder in the flat-space lattice is directly related to the curvature of the sphere on which the polytope sits.

The polytope is highly symmetrical; the disordered lattice has no symmetry at all. Still, depending on the form of the mapping, some of the symmetries may be approximately preserved. In the example shown, the fivefold rotational symmetry of the dodecahedron is approximately retained as a translational symmetry by lattice vector **a** in the patch of disordered lattice. We believe it is likely that this will be a general feature which carries over to more realistic cases: certain symmetries of the polytope will be approximately preserved locally upon mapping. In particular, rotational symmetries of the polytope will go over to approximate translational symmetries in flat space. Then, the quantum numbers labeling the irreducible representa-

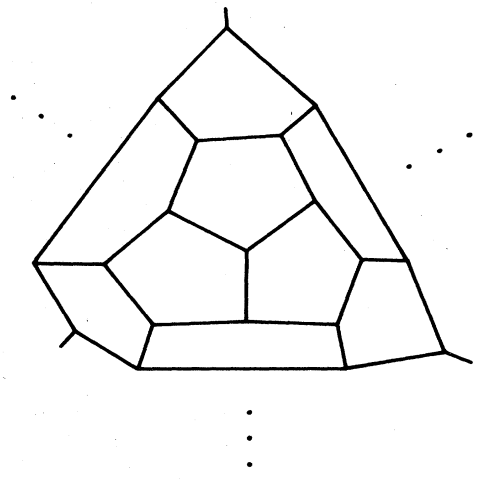

FIG. 4. An attempt to fill two-dimensional space using the rule, "Connect three pentagons at every vertex." This scheme for propagating short-range order is sensible locally, but becomes impossible in larger clusters.

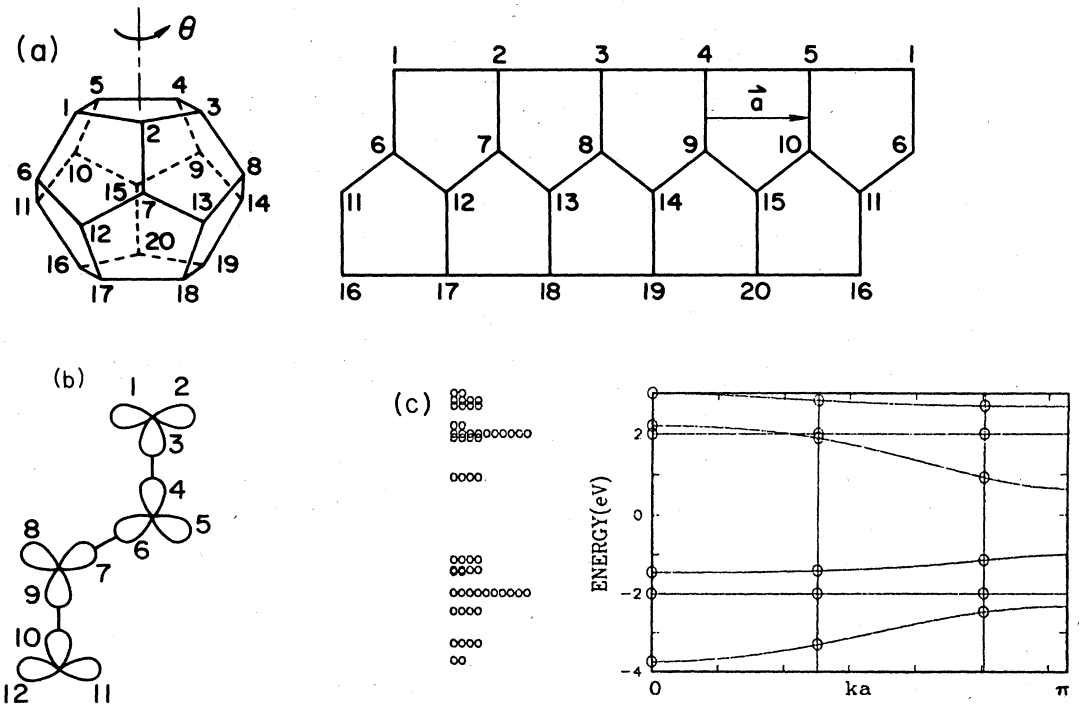

FIG. 5. (a) Perfect realization of the network-building rule of Fig. 4 on a curved two-dimensional space. The result is the familiar dodecahedron. This structure may be mapped onto flat two-dimensional space in any number of ways; one such way is shown on the right-hand side. In this mapping, the fivefold rotational symmetry of the dodecahedron around the axis $\hat{\theta}$ is approximately preserved as a translational symmetry **a**. (b) Our labeling of the twelve sp_2 tight-binding orbitals in one unit cell of the mapped structure in (a). (c) The resulting energy eigenvalue spectrum of the dodecahedron. On the left the states are shown in a molecular energy-level scheme, with the degeneracies indicated. The pseudotranslational symmetry of (a) permits these eigenvalues to be displayed as points on a continuous energy-band diagram. The dodecahedral eigenvalues occur where these bands cross the allowed **k** values as indicated.

tions of the relevant rotational subgroup of the polytope will go over (approximately) to a wave-vector-like index in flat space. In the 2D example shown, the cyclic group of order $n=5$ which corresponds to the rotational symmetries about the z axis is labeled by a quantum number m running from $m=0$ to $m=n-1=4$. The correspondence with a wave-vector index in real space is $2\pi m/na \rightarrow k$. This means that k runs roughly from 0 to $2\pi/a$, or $-\pi/a$ to π/a, which is just the dimension of a single Brillouin zone in a one-dimensional crystal. Of course, the wave vector takes on only a discrete set of values within this Brillouin zone. As we will show momentarily (see also Sec. IV), a simple analytic continuation is possible which permits quantities like the electronic energy states to be defined for any value of k,[14] and these may be relevant for patches of a random network like the one in Fig. 5(a) in which the pseudotranslational order in the **a** direction persists for more than n unit cells (i.e., more than five in this example).

We now work out a specific example of an electronic structure model on the polytope.[13] The calculation proceeds entirely by analogy with the usual crystal band-structure calculation. The unit cell contain four atoms labeled 4, 9, 14, and 19 in the figure; every other atom in the structure can be obtained from these by translation (or rotation in curved space). For our example we will use the tight-binding approximation,[15] assuming that the states of the polytope can be represented by sp_2 hybrids shown in Fig. 5(b). There are three such orbitals per atom, or 12 per unit cell, which are numbered in the figure. As usual in these calculations, this means that the calculation of electronic structure reduces to the finding that the solutions of a 12×12 secular equation $\det(\underline{H}-E\underline{S})=0$. In this case we will assume that the overlap matrix $\underline{S}$ is the identity. The Hamiltonian matrix elements between the sp_2 orbitals are given by a parameter V_1 for two different orbitals on the same atom, and by a parameter V_2 for two orbitals pointing towards each other from neighboring atoms [see Fig. 5(a)]. Since the basis functions are actually Bloch orbitals, differing by a phase factor $\exp(ika)$ from one unit cell to the next, the Hamiltonian matrix element picks up this phase (or its complex conjugate) when two interacting orbitals are in adjacent unit cells.

The resulting 12×12 Hamiltonian matrix is shown in Table I, and the resulting energy bands are shown in Fig. 5(c) with the choice of parameters $V_1=1$, $V_2=2$. Only half the Brillouin zone is shown; as usual, the bands have

TABLE I. sp_2 tight-binding Hamiltonian for the dodecahedron.

	1	2	3	4	5	6	7	8	9	10	11	12
1	0	$V_1+V_2e^{ika}$	V_1	0	0	0	0	0	0	0	0	0
2	$V_1+V_2e^{-ika}$	0	V_1	0	0	0	0	0	0	0	0	0
3	V_1	V_1	0	V_2	0	0	0	0	0	0	0	0
4	0	0	V_2	0	V_1	V_1	0	0	0	0	0	0
5	0	0	0	V_1	0	V_1	0	V_2e^{ika}	0	0	0	0
6	0	0	0	V_1	V_1	0	V_2	0	0	0	0	0
7	0	0	0	0	0	V_2	0	V_1	V_1	0	0	0
8	0	0	0	0	V_2e^{-ika}	0	V_1	0	V_1	0	0	0
9	0	0	0	0	0	0	V_1	V_1	0	V_2	0	0
10	0	0	0	0	0	0	0	0	V_2	0	V_1	V_1
11	0	0	0	0	0	0	0	0	0	V_1	0	$V_1+V_2e^{ika}$
12	0	0	0	0	0	0	0	0	0	V_1	$V_1+V_2e^{-ika}$	0

$\pm k$ symmetry. The discrete set of k values corresponding to allowed quantum numbers of the ideal polytope are indicated, and the "molecular" energy levels for the ideal polytope (symmetries disregarded) are shown on the left-hand side. The allowed energy levels have high degeneracy, much higher than can be explained by the k symmetry of the energy bands alone. This is simply a manifestation of the fact that we have not used all the symmetries of the polytope (i.e., the proper icosahedral group, of order 60) but only the rotational symmetries around one axis (a group of order five). We expect that some of the extra symmetries which lead to additional degeneracies are probably strongly broken by the mapping to flat space which we have chosen in Fig. 5(a). An important point is that the detailed form of the mapping determines which symmetries are preserved and which are broken. In the mapping chosen in Fig. 5(a), the fivefold axis is preserved; another choice of mapping could have preserved one of the threefold symmetries. [In fact, it would be more likely that a threefold symmetry would be approximately preserved in an arbitrary mapping than a fivefold symmetry, simply because there are more threefold axes (10) than fivefold axes (6).]

Figure 6(a) shows another such simple two-dimensional polytope, the cube. This structure results from the following rule for propagating SRO: join three four-sided figures at each vertex. In this case the sp_2 secular matrix is 8×8 (see Table II), and the resulting energy bands are

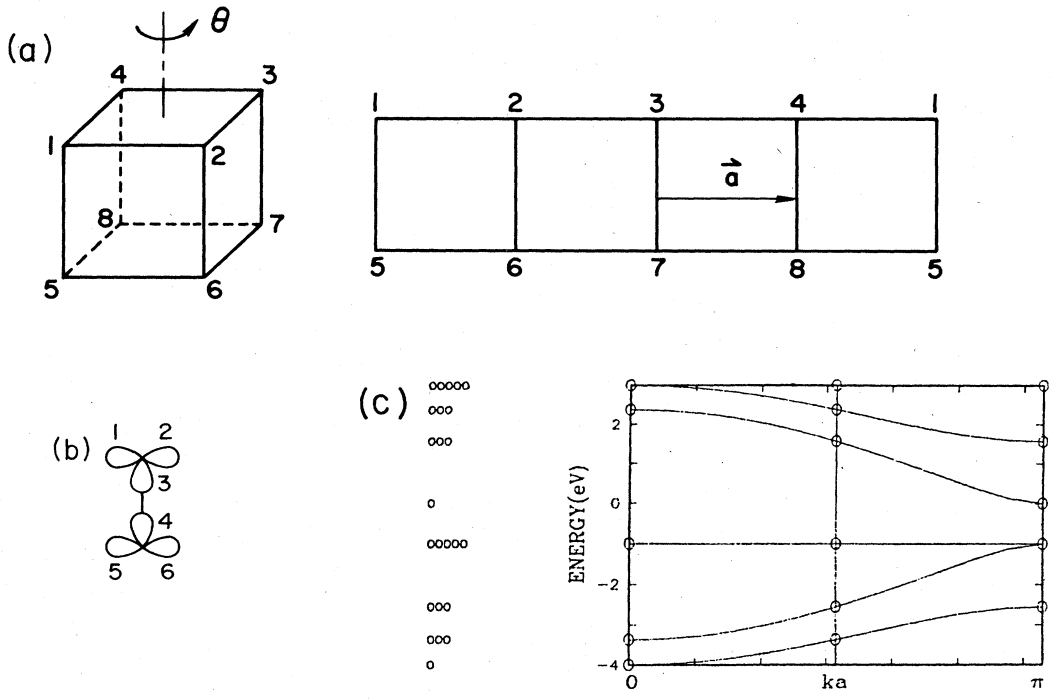

FIG. 6. (a) The result of applying the network-building rule, "Connect three squares at each vertex" (the cube, of course). (b) The six sp_2 tight-binding orbitals in the "unit cell" of the cube. (c) The energy eigenvalues displayed on a band structure.

TABLE II. sp_2 tight-binding Hamiltonian for the cube.

	1	2	3	4	5	6
1	0	$V_1+V_2e^{ika}$	V_1	0	0	0
2	$V_1+V_2e^{-ika}$	0	V_1	0	0	0
3	V_1	V_1	0	V_2	0	0
4	0	0	V_2	0	V_1	V_1
5	0	0	0	V_1	0	$V_1+V_2e^{ika}$
6	0	0	0	V_1	$V_1+V_2e^{-ika}$	0

shown in Fig. 6(c).

With this introduction, we move on to more realistic three-dimensional examples. These are more difficult to visualize, since the corresponding ideal polytope are wrapped onto a three sphere, which is embedded in *four*-dimensional Euclidean space. Nevertheless, the concepts we will use are very simple extensions of the ones introduced by these two-dimensional examples, and the reader will be aided by noting the analogies between two and three dimensions.

Before discussing some of the formal properties of the three-dimensional polytopes, let us briefly anticipate the results of the later sections of the paper (Secs. V and VI). In our applications of the polytope model to tetrahedrally-bonded amorphous solids, we will assume that the polytope generated by the rule "Place four *'petits barrelan'* around every vertex" (called polytope 240; see Fig. 3), is most representative of local order in the amorphous solid, so that clusters containing many atoms show the polytope-240 structure. There is one symmetry axis which occurs with the greatest frequency in polytope 240 (called the $\frac{30}{11}$ axis below); therefore, we will assume that the symmetry about this axis is the most nearly preserved upon mapping to flat space. Then, the energy eigenvalues of the amorphous solid can be organized into an energy-band structure by analogy to Figs. 5(c) and 6(c). When we say this, we ignore the presence of states associated with defects in the polytope-240 order. (We show in Appendix B that at least some kinds of defects do not introduce any important new electronic states.) Within this energy-band picture, we show that an approximate vertical selection rule for optical absorption is in force; a quantitative discussion of this appears in Sec. VI. We consider these optical selection rules as one possible reason for the small optical absorption near the fundamental band edge in hydrogenated amorphous Si and in well-annealed pure amorphous Si.[16]

III. SYMMETRY GROUPS OF THE POLYTOPES

In this section we give a complete and fairly formal discussion of the symmetry properties of the regular polytope. An understanding of these symmetries is quite useful in our modeling of amorphous solids. For example, we will exploit this symmetry to diagonalize model tight-binding Hamiltonians on the polytope lattice. The results of these calculations may be relevant to the local electronic structure in disordered solids, in which case the irreducible representations of these groups provide physically meaningful approximate indexing schemes for these local eigenstates. The polytope symmetries are also useful for indexing line defects in amorphous solids.[17]

A. The full symmetry groups

There are two mathematical accidents which make the structure and symmetries of the polytopes in positively-curved three-dimensional (3D) space (i.e., the three-sphere S^3) understandable entirely in terms of ordinary rotational symmetries in three dimensions. The first is that polytope coordinates, when written as four-dimensional vectors, may be viewed as unit quaternions. The multiplicative group of unit quaternions is isomorphic to SU(2), the covering group of SO(3). This implies a 2:1 homomorphism between the coordinates of the polytope and ordinary rotations in real space. The second accident is that SO(4), which is the group of all symmetry operations in the polytope space S^3, is isomorphic to $[SU(2)\times SU(2)]/\mathbb{Z}_2$, where $\mathbb{Z}_2$ is the two-element group. Therefore, because of the accidental relationships between different continuous groups, both the *vertex coordinates* and the *symmetry operations* of the polytopes are related to discrete subgroups of the ordinary 3D rotation group, lifted into the covering group SU(2). (This lifting results in groups which are often called "binary polyhedral groups" or "double groups.")

We now show explicitly the connection between the discrete rotational groups and the polytope vertices in a quaternion representation. We briefly review some properties of quaternions in Appendix A. (More information may be found in the books of DuVal[18] and Coxeter.[12,19]) The 2:1 homomorphism between Q (the group of quaternions) and SO(3) has a kernel which is generated by the quaternion -1. That is, the two different quaternions $\pm\exp(\alpha y)$ correspond to the same rotation by the angle 2α around a point y on the unit sphere. Here the quaternions are written in exponential notation (see Appendix A) and y is the unit pure quaternion which defines a point on the sphere S^2. For example, the image of the dihedral group D_2 (of order 4) is the group V' (of order 8) consisting of the 8 principal unit quaternions

$$(\pm 1,0,0,0),(0,\pm 1,0,0),(0,0,\pm 1,0),(0,0,0,\pm 1)\ . \qquad (1)$$

Note that each unit quaternion defines a point on the hypersphere S^3 of unit radius. The configuration of points corresponding to V' is the polytope $\{3,3,4\}$ (using standard notation[12]), sometimes called the hyperoctahed-

ron. Similarly, the lift of the tetrahedral group (of order 12) is the group T' (of order 24) which contains the group V' together with the 16 elements

$$\tfrac{1}{2}(\pm 1,\pm 1,\pm 1,\pm 1) . \tag{2}$$

Consequently T' can be written in the following standard form:[18]

$$T'=\bigoplus_{r=0}^{2}(\tfrac{1}{2},\tfrac{1}{2},\tfrac{1}{2},\tfrac{1}{2})^r V' , \tag{3}$$

where $\oplus_{r=1}^{n} A_r$ means the union of n sets A_r $(r=1,2,\ldots,n)$ which have no elements in common. The 24 elements of T' again correspond to a set of special points on S^3, the polytope $\{3,4,3\}$, which is a self-dual packing of octahedra.

We can go further and construct the groups O' and Y', the lifts of the octahedral and icosahedral groups, by further augmentation of the groups above. These can be written

$$O'=T'\oplus[T'\times(1/\sqrt{2})(1,1,0,0)] , \tag{4}$$

$$Y'=\bigoplus_{r=0}^{4}[T'\times(\tfrac{1}{2}\tau^{-1},-\tfrac{1}{2}\tau,0,-\tfrac{1}{2})^r] , \tag{5}$$

Here τ is the golden ratio: $\tau\equiv(1+\sqrt{5})/2$. The 120 elements of Y' correspond to the 120 vertices of polytope $\{3,3,5\}$ on S^3. Note that this systematic enumeration of all regular divisions of S^3 is about a century old.[20]

The symmetry groups of these polytopes, which are subgroups of SO(4), can also be specified within a quaternion representation because of the isomorphism $\mathrm{SO}(4)=[\mathrm{SU}(2)\times\mathrm{SU}(2)]/\mathbb{Z}_2$. This isomorphism is often explained by saying that any rigid displacement on the hypersphere S^3 is the product of a right screw and a left screw. Both the right and left screws form an SU(2) subgroup of the SO(4) symmetry group of S^3; thus the screw operations can be represented by quaternions. If $q\in Q$ denotes a point on S^3, the transformation

$$q\rightarrow lqr^{-1} \quad \text{with } l,r\in Q \tag{6}$$

is an element of SO(4). Pure rotations correspond to the "diagonal" case in Eq. (6), $l=r$. A "screw" is a transitive operation on S^3 with no points remaining invariant; a rotation leaves a plane invariant in the fourth dimension. Consider the following example. We present a unit quaternion by a pair of complex numbers (u,v) (see Appendix A). When S^3 is embedded in the fourth-dimensional (4D) Euclidean space $\mathbb{R}^4$ with axes w, x, y, and z, u and v represent complex coordinates in the planes wx and yz, respectively. A true rotation of angle α which leaves the plane wx invariant can be written as

$$(e^{i\alpha/2},0)(u,v)(e^{-i\alpha/2},0) . \tag{7}$$

Applying first the left screw, one obtains

$$(e^{i\alpha/2},0)(u,v)\rightarrow(e^{i\alpha/2}u,e^{i\alpha/2}v) . \tag{8}$$

This represents a simultaneous rotation by the angle $\alpha/2$ in the planes wx and yz. The application of the right screw, which corresponds to simultaneous rotations of $-\alpha/2$ in the plane wx and $+\alpha/2$ in the plane yz, gives

$$(e^{i\alpha/2}u,e^{i\alpha/2}v)(e^{-i\alpha/2},0)\rightarrow(u,e^{i\alpha}v) . \tag{9}$$

The net result is a "true" rotation of angle α in the plane yz which leaves the plane wx invariant.

This example illustrates operations in the direct product group $Q\times Q$, whose elements are the ordered pairs (l,r). The group has the multiplicative law

$$(l,r)(l'r')=(ll',rr'),\quad l,r,l',r'\in Q . \tag{10}$$

The 2:1 homomorphism between $Q\times Q$ and SO(4) has a kernel consisting of the pair of quaternions (1,1) and $(-1,-1)$. If as above we call this two-element group $\mathbb{Z}_2$, then SO(4) is isomorphic to $(Q\times Q)/\mathbb{Z}_2$. The discrete group of all direct rotations G' of polytope $\{3,3,5\}$ has a similar product structure:[18,17]

$$G'=(Y'\times Y')/\mathbb{Z}_2 . \tag{11}$$

A complete character table for the irreducible representations of G' is given by Warner.[21] The elements of G are given by the set of quaternion pairs (l,r), $(l,r\in Y')$, partitioned by the equivalence relation ξ

$$G'=(Y'\times Y')/\xi , \tag{12}$$

$$\xi:\ (l,r)\sim(l',r') \text{ if } \begin{cases} l=l' \text{ and } r=r' \\ l=-l' \text{ and } r=-r' . \end{cases}$$

Since the order of Y' is 120, Eqs. (11) and (12) imply that the order of G' is 7200. The total symmetry group G of polytope $\{3,3,5\}$ also includes indirect orthogonal transformations, analogous to reflections for ordinary 3D discrete groups. These are given by

$$q\rightarrow -l\bar{q}r,\quad l,r\in Y' . \tag{13}$$

This adds 7200 new elements since the equivalence relation ξ is still valid.

B. Description of polytope symmetries using the spherical torus

A particularly useful way of visualizing the space S^3 is as a set of coaxial tori. In this section we discuss the structure and symmetries of the polytopes using this description.

First we discuss the *spherical torus,* which is a special surface on S^3 defined by[19]

$$\begin{aligned} w&=\cos\alpha\cos\beta,\quad x=\cos\alpha\sin\beta , \\ y&=\sin\alpha\sin\beta,\quad z=\sin\alpha\cos\beta . \end{aligned} \tag{14}$$

Here $|\alpha+\beta|\leq\pi$. The spherical torus is a *developable* surface (i.e., it has zero Gaussian curvature at every point, in contrast to the classical torus in $\mathbb{R}^3$), since

$$\sum_{i=1}^{4} dx_i^2=d\alpha^2+d\beta^2 . \tag{15}$$

An alternative parametrization of the spherical torus which we shall use below is

$$w=\frac{1}{\sqrt{2}}\cos\psi,\quad x=\frac{1}{\sqrt{2}}\sin\psi\,,$$
$$y=\frac{1}{\sqrt{2}}\cos\phi,\quad z=\frac{1}{\sqrt{2}}\sin\phi \tag{16}$$

with $|\psi|,|\phi|\leq\pi$. This surface can be described as a square with opposite sides identified (Fig. 7). Any line parallel to one of the square diagonals becomes a great circle of S^3 (a geodesic line). There are also two important lines which correspond to the torus axes. For the classical torus in $\mathbb{R}^3$ these axes are a straight line and a circle. In the spherical torus case these lines are two nonintersecting great circles of S^3. Referred to the second parametrization of the spherical torus given above [Eq. (16)], the equations for these two lines are

$$w=0,\quad x=0\,, \tag{17}$$

and

$$y=0,\quad z=0\,. \tag{18}$$

In Fig. 8 we have shown a family of tori coaxial with the spherical torus. They have been projected according to the mapping

$$x_c=\frac{2x}{1-w}\,,\quad y_c=\frac{2y}{1-w}\,,\quad z_c=\frac{2z}{1-w}$$

between the S^3 coordinates w,x,y,z and the Cartesian coordinates of $\mathbb{R}^3$, x_c,y_c,z_c. The set of tori in Fig. 8 are characterized by the single parameter a in the equations

$$w=\sqrt{a}\,\cos\psi,\quad x=\sqrt{a}\,\sin\psi\,,$$
$$y=\sqrt{1-a}\,\cos\phi,\quad z=\sqrt{1-a}\,\sin\phi\,, \tag{19}$$

with $0<a<1$. $a=0.5$ is the spherical torus [see Eq. (16)].

The spherical torus surface partitions S^3 into two parts

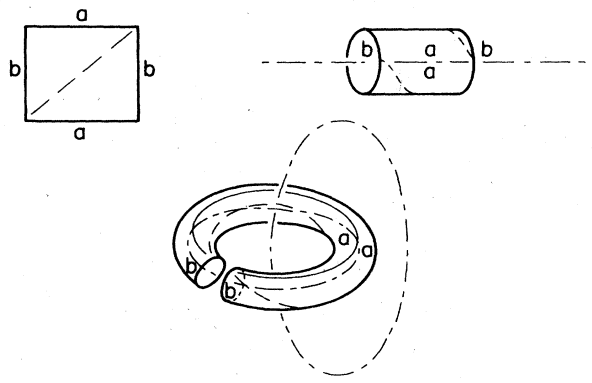

FIG. 7. Construction of the spherical torus. As for a normal torus, the spherical torus may be obtained by beginning with a square, then identifying opposite sides (the a's and the b's). Unlike the torus in flat space, the spherical torus in the three-sphere S^3 has zero curvature at every point. It divides the volume of S^3 into two equal parts. The two dotted-dashed lines are great circles of S^3 and they serve as axes of the spherical torus. The diagonal of the square (the dashed line) also becomes a great circle of S^3.

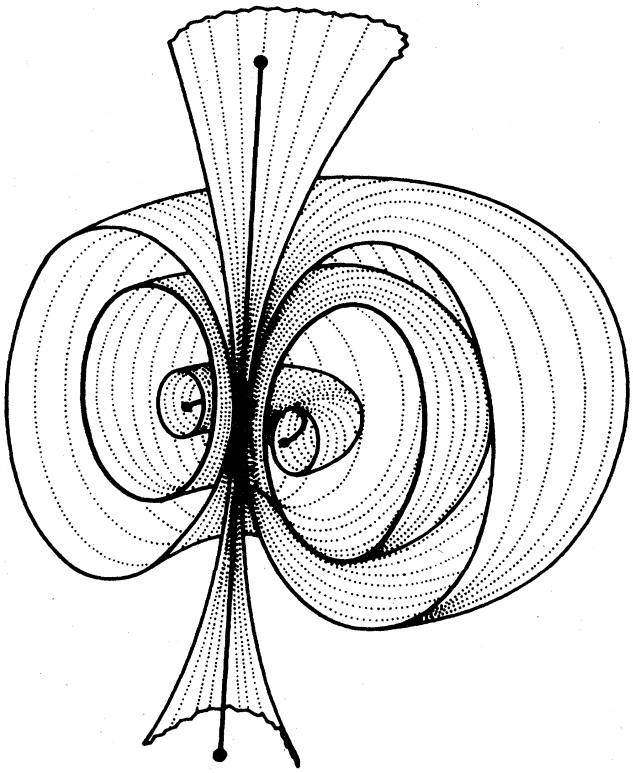

FIG. 8. Family of tori which are coaxial with the spherical torus. This family fills up the volume of the three-sphere S^3.

of equal volume. These are solid tori with the same two great circles as axes. Polytope vertices can be specified with respect to these tori once the spherical torus axis has been aligned with one of the polytope symmetry axes.

This can be illustrated in the simple case of the hypercube. A familiar projection of the hypercube in $\mathbb{R}^3$ is shown (as a projection in $\mathbb{R}^2$) in Fig. 9(a) in the form of a small cube inside of a larger one. This representation helps to illustrate those hypercube symmetries which can be described as rotations R_{wx} and R_{yz} on the torus surface. Successive applications of R_{wx} produce the rotations $1\rightarrow4\rightarrow8\rightarrow3\rightarrow1$ and R_{yz} the rotations $2\rightarrow5\rightarrow6\rightarrow7\rightarrow2$ of the 3-cube cells of the hypercube in Fig. 9(a). The hypercube is particularly simple because all of the vertices lie on the spherical torus surface [Fig. 9(b)]. In fact, it can be obtained by identification of opposite sides of a small portion of a square network, as shown in Fig. 10. Note that a different (but equivalent) choice of torus axes have been made in Fig. 10 as compared with Fig. 9.

From this construction, the hypercube may be viewed as a discretized approximation to the spherical torus. This discretization has an easy generalization. In the above example for the hypercube we started with a configuration containing 16 small squares (each long edge being divided into four short ones). If instead we start with a configuration containing 25 small squares, then after performing the wrapping procedure given in Fig. 10 one ob-

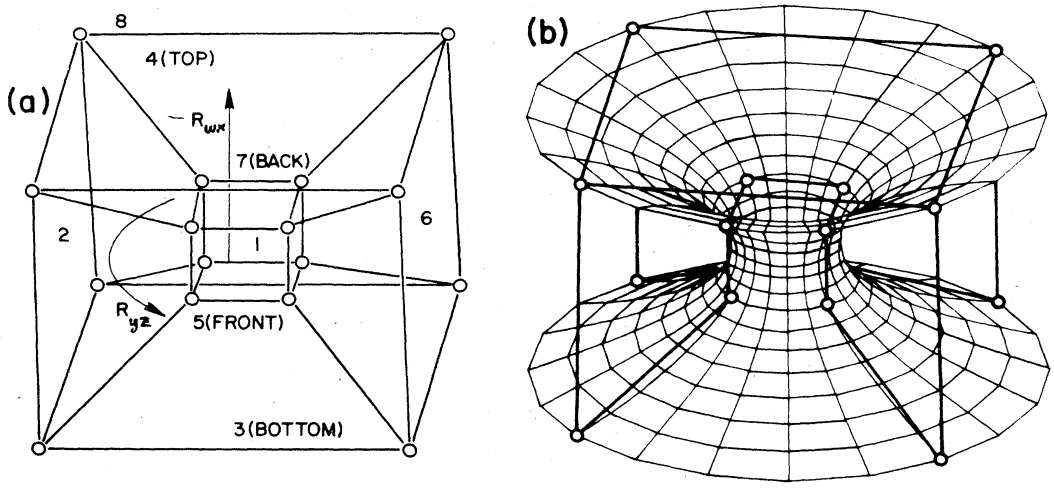

FIG. 9. (a) Hypercube (polytope $\{4,3,3\}$) in a conventional projection. The symmetries of the hypercube, and of the other polytopes, can be decomposed into rotations around (R_{yz}) and along (R_{wx}) the spherical torus, as described in the text. (b) The vertices all lie on the same spherical torus, as shown.

tains another approximation to the spherical torus surface shown in Fig. 11. In this case S^3 has been partitioned into pentagonal prisms. This discretization of the spherical torus is very similar to the approximation to the circle by polygons with a large number of edges; in this simple example the continuous symmetry of the circle, $U(1)$, is reduced to a finite-order group by the discretization.

The construction of Fig. 11 permits us to see the relationship of some of the other polytopes to the spherical torus. Figure 12 shows the manner in which the vertices of polytope $\{3,3,5\}$ are partitioned with respect to this pentagonal prismatic division of S^3. The local arrangement of dodecahedra in the dual polytope $\{5,3,3\}$ around the same axis is displayed in Fig. 13(a). The vertices of $\{5,3,3\}$ lie on several different toroidal surfaces surrounding this axis (see below). Note that as in the case of the hypercube, the torus axis corresponds to a symmetry axis of the polytope, in this case a ten-fold screw axis corresponding to simultaneous rotations of $2\pi/10$ around the two orthogonal planes defined by the torus axes. The surfaces containing the $\{5,3,3\}$ vertices are in general not the spherical (developable) torus, since they do not lie at equal distances from the two torus axes, although they are coaxial with it. They belong to the complete family of toroidal surfaces which fill up S^3 illustrated by Fig. 8.

The general conclusion is that, taking any screw or rotational axis of a given polytope, it is possible to decompose this symmetry into elementary rotations acting on two orthogonal planes, i.e., around and along the surfaces of Fig. 8. Pairs of great circles in S^3 define a spherical

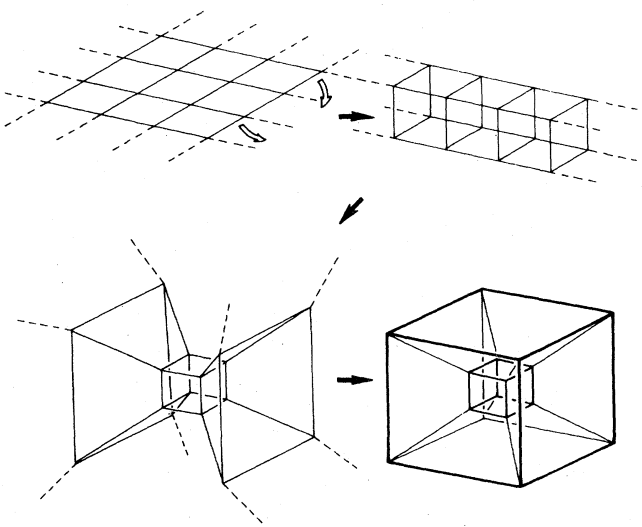

FIG. 10. The hypercube is obtained by applying periodic boundary conditions to a 4×4 piece of square lattice, as shown.

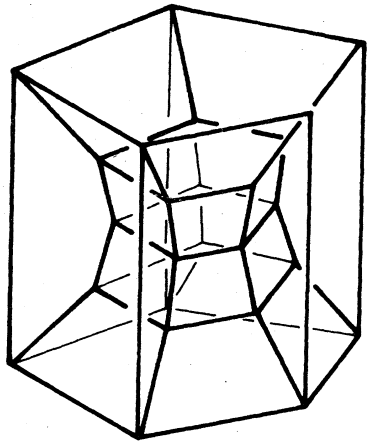

FIG. 11. Discrete approximation to the spherical torus by a set of pentagonal prisms. This structure may be obtained as in Fig. 10 by applying periodic boundary conditions to a 5×5 piece of square lattice.

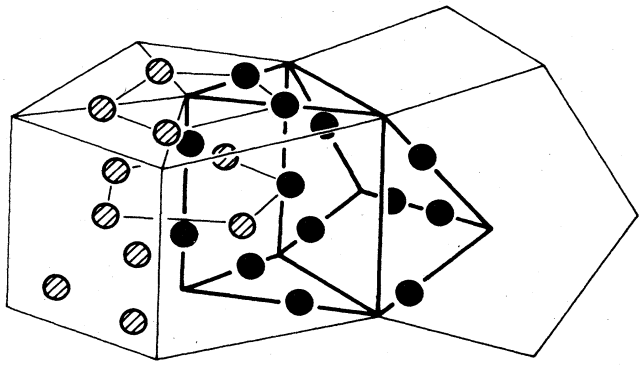

FIG. 12. Positions of the vertices of polytope {3,3,5} shown with respect to the pentagonal prismatic division of the three-sphere S^3 as shown in Fig. 11.

torus as well as a family of coaxial tori (Fig. 8) on which the polytope vertices are located. A suitable choice of the coordinate system makes these two orthogonal planes correspond with the planes wx and yz. We will show further examples of this construction for particular screw-symmetry axes of several polytopes. We will denote this screw-rotation symmetry, following the hypercube example above, as $[R_{wx}(\alpha), R_{yz}(\beta)]$, where $R_{wx}(\alpha)$ signifies a rotation by angle α in the plane wx which leaves the plane yz invariant. This specification of polytope symmetry operations is related to the quaternion representation described above in the following way. A point on S^3 denoted by the quaternion (u,v) $(u,v \in Q)$ is transformed into the points (u',v') under the rotation $R_{wx}(\alpha)$ in the following way:

$$(u',v')=(e^{i\alpha/2},0)(u,v)(e^{i\alpha/2},0) \\ =(ue^{i\alpha},v) . \tag{20}$$

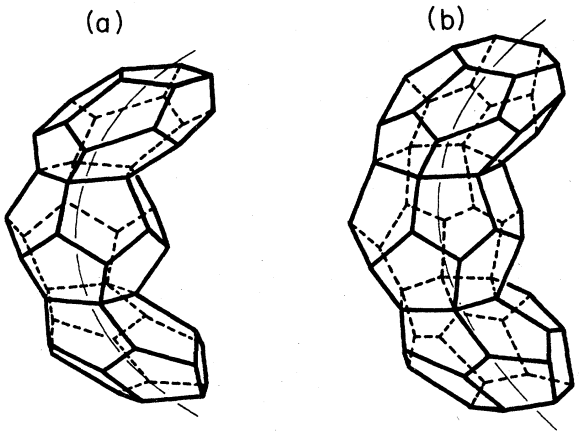

FIG. 13. (a) Projection of the vertices {5,3,3}. {5,3,3} consists of a packing of dodecahedra; the configuration of a few of these dodecahedra about one of the torus axes is shown. (b) Same torus axis after the insertion of a $-72°$ disclination line.

This quaternion operation clearly describes a rotation in the plane wx which leaves yz invariant. Similarly the application of $R_{yx}(\beta)$ gives

$$(u',v')=(e^{i\beta/2},0)(u,v)(e^{-i\beta/2},0) . \tag{21}$$

So a general transformation $(R_{wx}(\alpha), R_{yz}(\beta))$ reads

$$(u',v')=(e^{i(\alpha+\beta)/2},0)(u,v)(e^{i(\alpha-\beta)/2},0) . \tag{22}$$

When $\alpha=\beta$ one obtains a left screw, simultaneous rotations of the same angle in two orthogonal planes. The point of this new description of transformations on S^3 is that it is always possible to find two complete orthogonal planes π_1, π_2 for which a given element of SO(4) is expressed as successive simple rotations in these two planes. This fact is a great aid to the visualization of SO(4) symmetry operations in S^3. Using this new notation we examine several of the polytopes.

C. Polytope {4,3,3} (the hypercube)

{4,3,3} has 16 vertices. It may be built according to the SRO propagation rule, "Fit four cubes around each vertex." In a suitable coordinate system these vertices are specified by permutations of

$$(\pm\tfrac{1}{2},\pm\tfrac{1}{2},\pm\tfrac{1}{2},\pm\tfrac{1}{2}) , \tag{23}$$

which can also be written (see Appendix A),[19]

$$\frac{1}{\sqrt{2}}(e^{i\pi(2\mu+1)/4},e^{i\pi(2\nu+1)/4}),\ \mu,\nu=0,1,2,3 . \tag{24}$$

From this equation it is evident that the {4,3,3} possesses the following rotational symmetries $(R_{wx}(\alpha), R_{yz}(\beta))$:

$$\left.\begin{aligned}\alpha&=m\pi/2\\ \beta&=n\pi/2\end{aligned}\right\}\ m,n=0,1,2,3 . \tag{25}$$

The sixteen vertices of this polytope belong to the spherical torus specified by Eq. (22) whose generic point (u,v) is such that $|u|=|v|=\sqrt{1/2}$.

D. Polytope {3,3,5}

This is generated by the rule, "Place 20 tetrahedra around each vertex." We will give here two sets of coordinates for the polytope. They are related by a rigid displacement on S^3 and can also be derived from the coordinate set associated with the group Y' [denoted $\{(u,v)_{Y'}\}$—see Eq. (5)].

The first set [denoted $\{(u,v)_{\mathrm{I}}\}$] is such that the {3,3,5} vertices are disposed with respect to the two fivefold "axes" in the planes wx and yz. As discussed above, these two axes generate a pentagonal prismatic division of S^3. The way that the vertices are arranged within the pentagonal prisms is shown in Fig. 12. Coordinates are given[19] in the following form:

$$(u,v)=\begin{cases}(\epsilon^{2\mu+1},0),\\ (\epsilon^{2\mu}\cos\lambda,\epsilon^{2\nu}\sin\lambda), & \mu+\nu \text{ even},\\ (\epsilon^{2\mu}\sin\lambda,\epsilon^{2\nu}\cos\lambda), & \mu+\nu \text{ odd},\\ (0,\epsilon^{2\nu+1}),\end{cases} \tag{26}$$

where $\epsilon\equiv\exp(i\pi/10)$, $\lambda\equiv\frac{1}{2}\tan^{-1}2$, and μ and ν run independently over the values $0,1,\ldots,9$. It is easily verified with this explicit coordinate specification that this polytope admits the symmetries $[R_{wx}(\alpha), R_{yz}(\beta)]$ in the planes wx and yz with

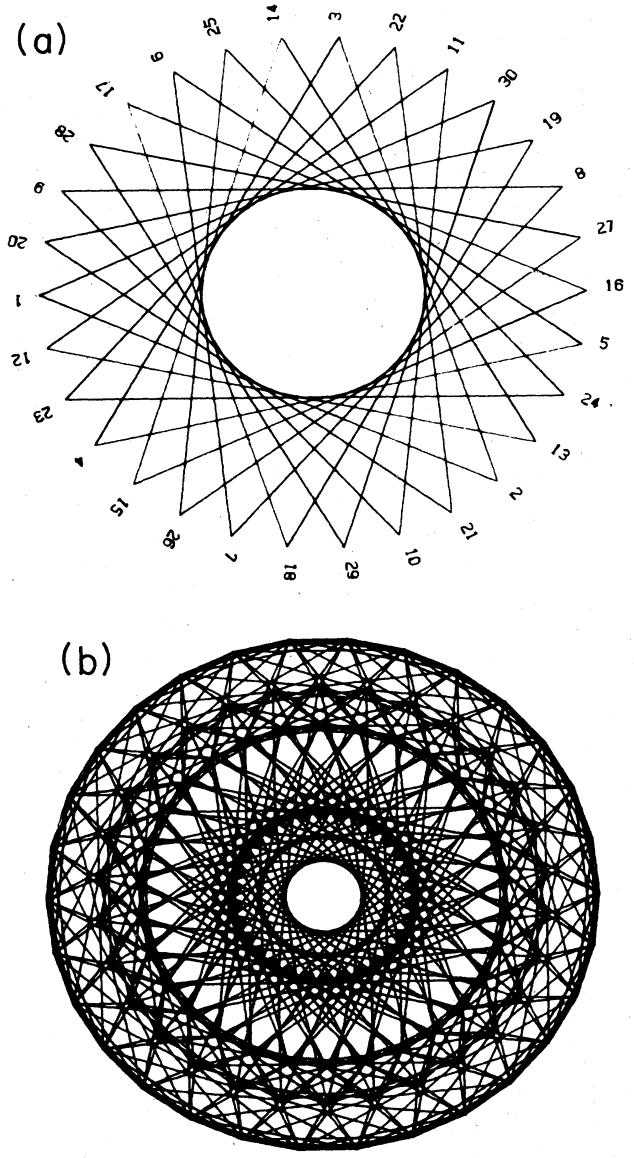

FIG. 14. (a) The $\{\frac{30}{11}\}$ polygon resulting from an orthogonal projection of a subset of the $\{3,3,5\}$ vertices along the $\frac{30}{11}$ axis. (b) The same projection including *all* of the vertices and nearest-neighbor bonds.

$$\left.\begin{aligned}\alpha&=m\,2\pi/5\\ \beta&=n\,2\pi/5\end{aligned}\right\}\ m,n=0,1,2,3,4\ . \tag{27}$$

These rotations transform a vertex (u,v) according to

$$(u,v)\rightarrow(\epsilon^{2(m+n)},0)(u,v)(\epsilon^{2(m-n)},0)\ . \tag{28}$$

Notice that in addition to this symmetry there is also a left tenfold screw axis:

$$\left.\begin{aligned}\alpha&=p\,2\pi/10\\ \beta&=p\,2\pi/10\end{aligned}\right\}\ p=0,1,\ldots,9\ , \tag{29}$$

which will be useful later. The correspondence between the sets $\{(u,v)_{Y'}\}$ and $\{(u,v)_{\rm I}\}$ can be written

$$\{(u,v)_{\rm I}\}=\left[\epsilon^{-1}\cos\frac{\lambda}{2},-\epsilon^{-1}\sin\frac{\lambda}{2}\right]\{(u,v)_{Y'}\}\times\left[\cos\frac{\lambda}{2},\sin\frac{\lambda}{2}\right]\ . \tag{30}$$

The second set of coordinates, denoted $\{(u,v)_{\rm II}\}$, is associated with the "triacontal" axis of polytope $\{3,3,5\}$ (Ref. 12). The 120 vertices belong to 4 sets A, B, C, and D of 30 vertices each given by

$$\begin{aligned}A_m&=[a\exp(i\pi m\tfrac{1}{30}),d\exp(i\pi m\tfrac{11}{30})]\ ,\\ &\qquad m(\text{even})=0,2,\ldots,58\\ B_m&=[b\exp(i\pi m\tfrac{1}{30}),c\exp(i\pi m\tfrac{11}{30})]\ ,\\ &\qquad m(\text{odd})=1,3,\ldots,59\\ C_m&=[c\exp(i\pi m\tfrac{1}{30}),-b\exp(i\pi m\tfrac{11}{30})]\ ,\\ &\qquad m(\text{odd})=1,3,\ldots,59\\ D_m&=[d\exp(i\pi m\tfrac{1}{30}),-a\exp(i\pi m\tfrac{11}{30})]\ ,\\ &\qquad m(\text{even})=0,2,\ldots,58\end{aligned} \tag{31}$$

where

$$\begin{aligned}a&=[(\tfrac{1}{2})(1+3^{-1/2}5^{-1/4}\tau^{3/2})]^{1/2}\ ,\\ b&=[(\tfrac{1}{2})(1+3^{-1/2}5^{-1/4}\tau^{-3/2})]^{1/2}\ ,\\ c&=[(\tfrac{1}{2})(1-3^{-1/2}5^{-1/4}\tau^{-3/2})]^{1/2}\ ,\\ d&=[(\tfrac{1}{2})(1-3^{-1/2}5^{-1/4}\tau^{3/2})]^{1/2}\ .\end{aligned} \tag{32}$$

Again τ is the golden ratio $\tau=(1+\sqrt{5})/2$. The coordinate sets I and II are related by

$$\{(u,v)_{\rm II}\}=\{(u,v)_{\rm I}\}(a,d)\ . \tag{33}$$

From these coordinates it is easy to see that the polytope possesses a particular screw symmetry:

$$\left.\begin{matrix} 2\pi p\frac{1}{30} \\ 2\pi p\frac{11}{30} \end{matrix}\right\} p=1,2,\ldots,30\ . \tag{34}$$

Each subset of points A_i, B_j, C_k, and D_l belongs to a torus with principal axes in the planes wx and yz. It is clear that the whole set of $\{3,3,5\}$ vertices can be generated as the orbit, under the screw operation of Eq. (34), of the four points A_0, B_1, C_1, and D_0. When mapped onto the wx plane each orbit gives a triacontagon (a simple polygon with 30 edges); when mapped onto the yx plane, each gives a triacontagram [see Fig. 14(a)]. A triacontagram (denoted $\{\frac{30}{11}\}$ by Ref. 12) is such that by passing around its 30 edges one has rotated exactly 11 times 2π. The complete mapping of polytope $\{3,3,5\}$ on either the plane wx or yz, with all vertices and edges, is shown in Fig. 14(b). The configuration of vertices on the torus surface nearest the plane yz is similar to that of a linear arrangement of tetrahedra described by Bernal[22] (Fig. 15). If one forms such a linear arrangement of 28 tetrahedra (in Euclidean space), the 31st vertex has roughly the same angular coordinate (in a cylindrical coordinate system) as the first vertex (Ref. 23). There is a small angular misfit of 5°40′ which disappears when the space is curved. These two vertices then coincide on S^3.

E. Polytope $\{5,3,3\}$

$\{5,3,3\}$ results from the rule, "Put four dodecahedra around each vertex." It is dual to polytope $\{3,3,5\}$, which permits us to obtain one coordinate set as follows.[18] Let us call I the set of $\{3,3,5\}$ vertices given by Y' $[I=\{(u,v)_{Y'}\}]$, t the quaternion $(e^{i\pi/4},0)$, and p an element of order 5 in Y', e.g., $p=\frac{1}{2}(\tau^{-1},\tau,0,1)$. Then the sets $\{\bar{I}\}$ and $\{\bar{\bar{I}}\}$ given by

$$\begin{aligned} \bar{I}_j &= p^j t I\ , \\ \bar{\bar{I}}_k &= I t p^{-k}\ , \end{aligned} \tag{35}$$

define new versions of polytope $\{3,3,5\}$ on S^3 with different orientations. Then the set J:

$$J=\bigoplus_{j=0}^{4}\bar{I}_j=\bigoplus_{k=0}^{4}\bar{\bar{I}}_k \tag{36}$$

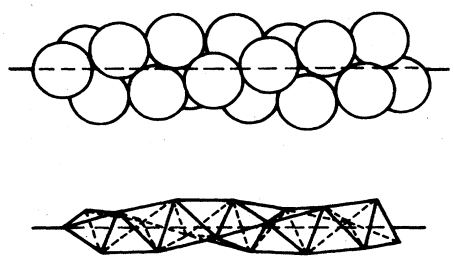

FIG. 15. Linear arrangement of tetrahedra along the $\frac{30}{11}$ axis of $\{3,3,5\}$, called the Bernal spiral (Ref. 22).

contains 600 vertices which form the polytope $\{5,3,3\}$. Since $\{5,3,3\}$ and $\{3,3,5\}$ have the same symmetry group, the coordinate sets $\{(u,v)_{\mathrm{I}}\}$ and $\{(u,v)_{\mathrm{II}}\}$ (associated with the fivefold and $\{\frac{30}{11}\}$ axes, respectively) for $\{5,3,3\}$ are derived from the set J in the same way as these sets are derived from $\{(u,v)_{Y'}\}$ for $\{3,3,5\}$.

F. Polytope 240

This tetracoordinated polytope with 240 vertices has been presented elsewhere.[6,7] It is generated by the rule mentioned in the Introduction: "Place four *'petits barrelans'* around each vertex." While polytope 240 was rediscovered only quite recently, it was first reported in the mathematical literature some 55 years ago.[24] The relation between it and $\{3,3,5\}$ is very similar to that between the diamond and fcc lattices. While the diamond crystal contains two interpenetrating fcc lattices displaced in the (111) direction, polytope 240 contains two versions of $\{3,3,5\}$ related by a screw operation. If one sublattice is specified by $\{(u,v)_{Y'}\}$, then one choice of the screw operation generating the other sublattice is $[\exp(i\pi/4),0]$. This can be applied as either a left or right screw; these operations generate equivalent but enantiomorphic structures (i.e., of the opposite chirality; see below). The new 120 vertices belong to the polytope $\{5,3,3\}$ described above and are located at the centers of the tetrahedral cells of $\{3,3,5\}$. (One out of every five $\{3,3,5\}$ cells is centered.) There are several equivalent ways of selecting these 120 tetrahedral cells among the 600 cells of $\{3,3,5\}$ (or equivalently, to select the appropriate 120 vertices among the 600 vertices of polytope $\{5,3,3\}$). Using the same notation as above, ten equivalent sets P of polytope 240 vertices (actually 5 chiral pairs) can be written

$$\begin{aligned} &P=I\oplus\bar{I}_j,\quad j=0,\ 1,\ 2,\ 3,\ \text{or}\ 4 \\ &\text{or} \\ &P=I\oplus\bar{\bar{I}}_k,\quad k=0,\ 1,\ 2,\ 3,\ \text{or}\ 4\ . \end{aligned} \tag{37}$$

If one takes the coordinate set

$$P=I\oplus\bar{\bar{I}}_1\ \text{ or }\ P=I\oplus\bar{\bar{I}}_4 \tag{38}$$

for polytope 240, the above-mentioned transformations can be used to get the sets $\{(u,v)_{\mathrm{I}}\}$ and $\{(u,v)_{\mathrm{II}}\}$. The vertices in $\{(u,v)_{\mathrm{II}}\}$ are located on the same four torus surfaces as the $\{3,3,5\}$ vertices. The yz torus axis remains a $\{\frac{30}{11}\}$ screw axis, and the atoms in the torus nearest this axis [shown in Fig. 16(a)] have the appearance of a channeling axis. The complete mapping of polytope 240 (with edges and vertices) is shown in Fig. 16(b).

The complete symmetry group of polytope 240 is clearly no longer $G'=(Y'\times Y')/\mathbb{Z}_2$ as for $\{3,3,5\}$ or $\{5,3,3\}$. The local icosahedral rotational symmetry of $\{3,3,5\}$ is broken down to a local tetrahedral rotation symmetry in the tetracoordinated polytope 240. On this basis one might guess that polytope 240 is invariant under a subgroup of G', $(T'\times Y')/\mathbb{Z}_2$, where T' is the lift of the tetrahedral group. We have found numerically that this is indeed the case. $(T'\times Y')/\mathbb{Z}_2$ would in fact be the full symmetry group if the two $\{3,3,5\}$ sublattices were distin-

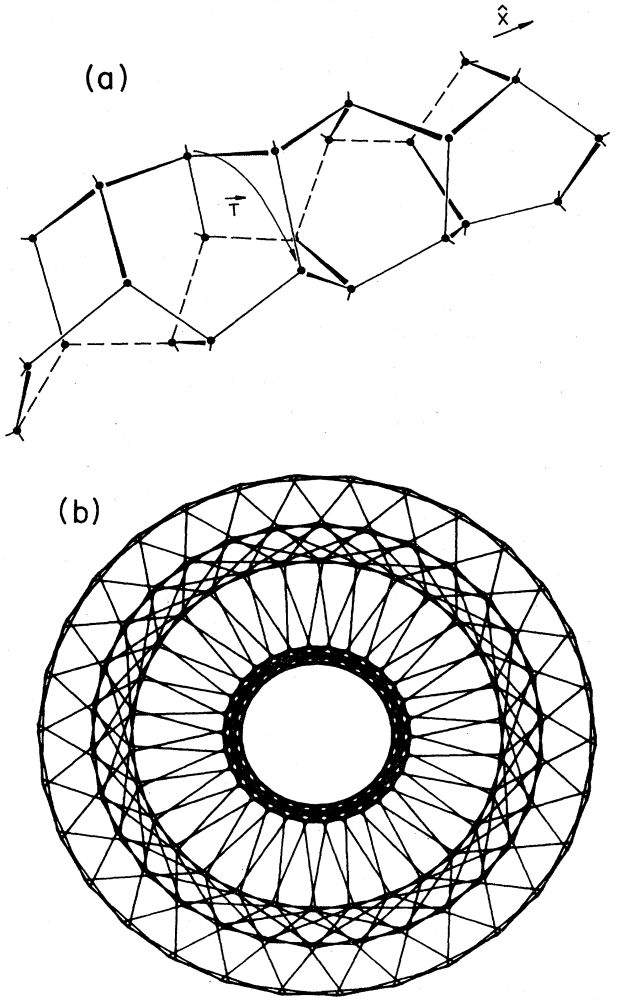

FIG. 16. (a) View of the atoms around the $\frac{30}{11}$ axis in polytope 240. The structure consists of three (110)-like chains which are bonded together and spiraling around the central axis; one of these chains is shown dashed. The operation denoted **T** is the $\frac{30}{11}$ symmetry rotation. (b) Orthogonal projection of the entire polytope 240 along the $\frac{30}{11}$ axis. This may be compared with Fig. 14(b).

guishable. Since they are not, there is one further symmetry generator corresponding to an interchange of the two sublattices. The resulting total symmetry group is $(O'\times Y')/\mathbb{Z}_2$, where O' is the lift of the octahedral group. This group is of order 2880. Note the asymmetry between left-hand and right-hand screws; this is a signature of the chirality of the structure. [The symmetry group of the polytope of the opposite handedness is $(Y'\times O')/\mathbb{Z}_2$.] As mentioned above, the 30-fold screw symmetry is preserved, since it is made up of the lift of threefold left screws from O' and the lift of fivefold right screws from Y'. There is another high symmetry screw axis in polytope 240 which has no counterpart in $\{3,3,5\}$, which is composed of the lift of the fourfold left screws from O'

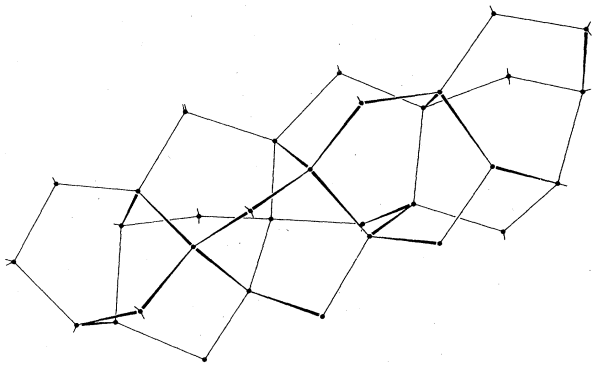

FIG. 17. View of the atoms around the $\frac{40}{9}$ axis in polytope 240.

and the lift of fivefold right screws from Y'. In our previous notation, the screw symmetry group about this axis is

$$\left.\begin{aligned}\alpha&=2p\pi\tfrac{1}{40}\\ \beta&=2p\pi\tfrac{9}{40}\end{aligned}\right\}p=0,1,2,\ldots,39\ . \tag{39}$$

The structure of the vertices around the corresponding torus axes is shown in Fig. 17. We will refer to this below as the $\{\frac{40}{9}\}$ axis.

IV. THE *s*-BAND SPECTRUM OF THE POLYTOPES

Following the work of Sec. II, in this section we compute the electronic spectrum of some of the polytopes within a tight-binding *s*-orbital approximation. Our purpose is to illustrate some of the concepts of electronic structure which will be useful for the more realistic case considered in the next section. We show how the electronic structures can be simplified by considering certain subgroups of the polytope symmetries; this will be relevant since we will show later how the SO(4) symmetries possessed by the ideal polytope could be relevant as pseudosymmetries of lattice structures in real space.

A. The hypercube {4,3,3} spectrum

Consider a hypercube with the coordinate set defined in the preceding section. There are two independent fourfold symmetry axes in the planes wx and yz. The rotation R_{wx} partitions the 16 $\{4,3,3\}$ vertices into four sets which transform only among themselves under the rotation. If one uses only the R_{wx} symmetry, the 16×16 *s*-band Hamiltonian matrix may be reduced to a 4×4 secular matrix, with one row (or column) for each of these four sets of vertices. To obtain the *s*-band eigenvalues, this matrix must be diagonalized at four points in the pseudo-Brillouin zone

$$k_1=\frac{2\pi m}{4a},\quad m=0,1,2,3\ . \tag{40}$$

Here a is the geodesic distance between nearest-neighbor vertices. The k_1's simply label the irreducible representations of the cyclic Abelian group generated by R_{wx}, as explained in Sec. II. If we use R_{wx} along with the second fourfold rotation R_{yz}, any vertex may be rotated into any other vertex. As a consequence the s-band Hamiltonian matrix becomes a trivial 1×1. This Hamiltonian must be "diagonalized" for every pair (k_1,k_2), where

$$k_2=\frac{2\pi p}{4a},\quad p=0,1,2,3 \tag{41}$$

labels the irreducible representations of the group generated by R_{yz}. We have thus succeeded in completely diagonalizing the Hamiltonian for $\{4,4,3\}$ by using the direct product symmetry group generated by the two fourfold rotations. As discussed in Sec. II, the labels of the representations of this group may be represented as discrete points within a continuous two-dimensional Brillouin zone. The eigenvalues are given by the expression

$$E=2[\cos(k_1a)+\cos(k_2a)]\,, \tag{42}$$

with k_1 and k_2 taking on the allowed values mentioned above. Here we take the hopping matrix element to be unity. Viewed as a continuous function in the 2D $\mathbf{k}$ space, this expression just gives the energy band of an infinite square lattice. This is not surprising since, as we have shown, the $\{4,3,3\}$ is topologically equivalent to a 4×4 piece of a square lattice with periodic boundary conditions.

B. The polytope $\{3,3,5\}$

Here we will exploit the $\{\frac{30}{11}\}$ screw symmetry about the triacontal axis of the polytope to partially diagonalize the s-band Hamiltonian. This symmetry partitions the vertex set into four subsets A_m, B_m, C_m, and D_m [Eqs. (31)]. The four vertices A_0, B_1, C_1, and D_0 (whose orbit under the screw operation gives the 120 polytope $\{3,3,5\}$ vertices) belong to a "unit cell." In order to construct the resulting 4×4 secular matrix we need to know which of the members of these sets are connected by bonds, either from different sets or within the same set. These are

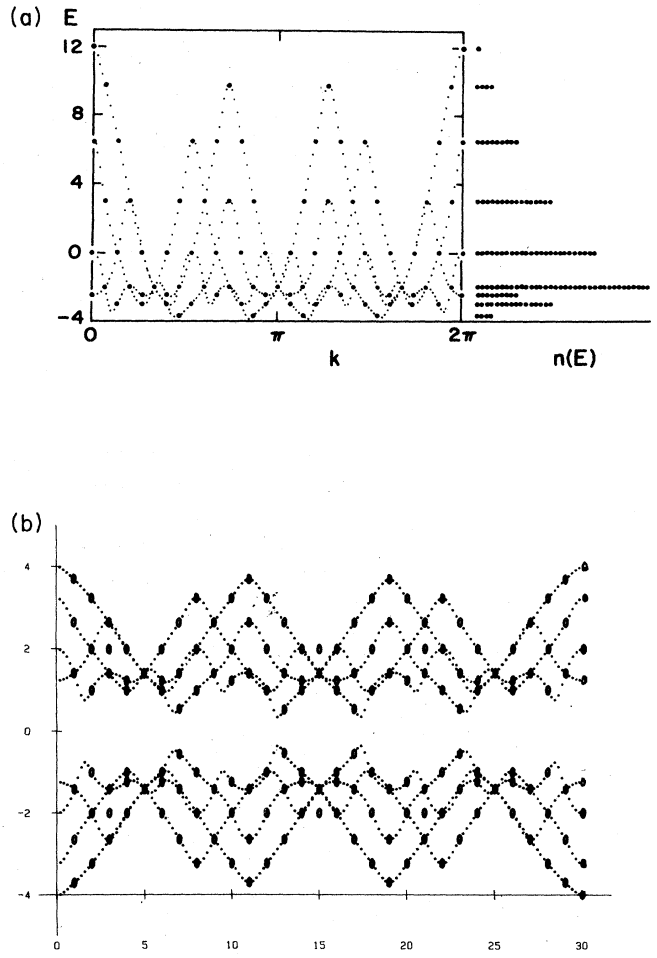

FIG. 18. (a) Energy bands of an s-band Hamiltonian applied to polytope $\{3,3,5\}$. The wave vector corresponds to the $\frac{30}{11}$ symmetry. The density of states, obtained by projecting the allowed states in the band structure (solid circles) horizontally, is shown on the right. (This may be compared with Fig. 5 of Ref. 17). (b) The s-state $\frac{30}{11}$ energy bands for polytope 240. The similarity between (a) and (b) is explained by Eq. (45) in the text.

TABLE III. s-band Hamiltonian for polytope $\{3,3,5\}$.

$2[\cos(2ka)+\cos(4ka)+\cos(6ka)]$	$2[\cos(ka)+\cos(5ka)]$	$2\cos(3ka)$	0
$2[\cos(ka)+\cos(5ka)]$	$2\cos(6ka)$	$2[\cos(2ka)+\cos(6ka)]$	$2\cos(3ka)$
$2\cos(3ka)$	$2[\cos(2ka)+\cos(8ka)]$	$2\cos(6ka)$	$2[\cos(5ka)+\cos(11ka)]$
0	$2\cos(3ka)$	$2[\cos(5ka)+\cos(11ka)]$	$2[\cos(6ka)+\cos(16ka)+\cos(22ka)]$

given by Coxeter[12] in the form:

$$\begin{aligned}
&A_jA_k, \quad |j-k| = 2 \text{ or } 4 \text{ or } 6 \pmod{60}\\
&A_jB_k, \quad |j-k| = 1 \text{ or } 5\\
&A_jC_k, \quad |j-k| = 3\\
&B_jB_k, \quad |j-k| = 6\\
&B_jC_k, \quad |j-k| = 2 \text{ or } 8\\
&B_jD_k, \quad |j-k| = 3\\
&C_jC_k, \quad |j-k| = 6\\
&C_jD_k, \quad |j-k| = 5 \text{ or } 11\\
&D_jD_k, \quad |j-k| = 6 \text{ or } 16 \text{ or } 22\ .
\end{aligned} \tag{43}$$

From this information, the matrix elements between the "Bloch orbitals" are easily constructed, leading to the secular equation in Table III. The Brillouin zone is one dimensional with the allowed k values given by

$$k = \frac{n\pi}{30a}, \quad n = 0,1,\ldots,29\ . \tag{44}$$

The band diagram is shown in Fig. 18 together with the resulting density of states. A more complete analysis of the eigenvalue spectrum of $\{3,3,5\}$ has been performed by Widom and Nelson,[17,25] who show that the secular matrix can be completely diagonalized if all of the symmetries of $\{3,3,5\}$ are used.

C. The polytope 240 spectrum

We again pick out the $\{\frac{30}{11}\}$ screw axis with the coordinate set $I \oplus \bar{\bar{I}}_1$ or $I \oplus \bar{\bar{I}}_4$. The "unit cell" contains eight sites (four atom each $\{3,3,5\}$ subset). We must choose a phase convention in which the members of the sets I and $\bar{\bar{I}}$ which map onto one another have the same Bloch phase factor (i.e., we must choose which atoms belong to the same "unit cell"). With the coordinate set as chosen, each of the four toroidal surfaces contains a set of 30 vertices from I and another from $\bar{\bar{I}}$. A convenient one-to-one mapping between sets I and $\bar{\bar{I}}$ can be established by arbitrarily identifying first-neighbor sites on each toroidal surface [e.g., the channeling axis in Fig. 16(a)]. The resulting secular matrix is given in Table IV. The 30 allowed $\mathbf{k}$ values are the same as for polytope $\{3,3,5\}$ [Eq. (44)]. The eigenvalue spectrum of polytope 240 is shown in Fig. 19(a). A very simple relationship may be demonstrated between the polytope 240 eigenvalues and those of $\{3,3,5\}$ (Ref. 26), which is a general consequence of the "alternant" structure of the lattice.[27] For every $\mathbf{k}$,

$$E_{240} = \pm(4 + E_{120})^{1/2}\ . \tag{45}$$

This relationship is evident in Figs. 18 and 19. The "alternant" or "bipartite" structure of the polytope (each vertex of set I has its four-nearest neighbors in set $\bar{\bar{I}}$ and vice versa) has two main effects. (1) The spectrum is symmetrical about zero; odd moments of the spectrum vanish since there are no odd-membered rings. (2) A completely antibonding eigenstate is supported by polytope 240—the "antibonding edge"[28] is attained— since all rings are even. Note that the antibonding limit for $\{3,3,5\}$, which would be at $E=-12$ in Fig. 18(a), is *not* attained, since the smallest rings are odd-membered (3). A sp_3 spectrum for polytope 240 may be derived through the Weaire-Thorpe transformation;[28] a more accurate treatment of the sp_3 band will be given in Sec. V.

D. The polytope $\{5,3,3\}$ spectrum

We will partially diagonalize the Hamiltonian for this structure by using the symmetries contained in the direct product group generated by the fivefold rotation and the tenfold screw axis described in Sec. III. This choice results in the smallest matrix size (12×12) consistent with our wave-vector—indexing scheme. (Use of the $\{\frac{30}{11}\}$ axis would have resulted in a 20×20 matrix.) In other words, there are 12 sets of vertices which transform among themselves under the action of the group. Using the same sort of analysis as we have discussed above, we obtain the 12×12 matrix shown in Table V. It contains many zeros because the vertices are grouped onto seven toroidal surfaces surrounding the fivefold axis. Nearest neighbors belong either to the same toroidal surface or to adjacent surfaces; many of the vertex sets are therefore not nearest neighbors. To be more specific, the 12 sets of vertices are organized such that there is one set on the surface nearest the fivefold axis, two sets on each of the next five surfaces, and one set on the last surface (which surrounds the complementary fivefold axis). Note that the fourth torus surface is a spherical torus, i.e., it is equidistant from the two fivefold axes. The vertices of the polytope on the spherical torus are arranged in a square lattice configuration but are not nearest neighbors. This explains the null 2×2 central block of Table V. The allowed $\mathbf{k}$ points in the (two-dimensional) Brillouin zone for this case are

TABLE IV. s-band Hamiltonian for polytope 240.

0	$1+e^{4ika}+e^{6ika}$	0	e^{5ika}	0	0	0	0
$1+e^{-4ika}+e^{-6ika}$	0	e^{-5ika}	0	0	0	0	0
	e^{5ika}	0	1	0	$e^{2ika}+e^{8ika}$	0	0
e^{-5ika}	0	1	0	$e^{-2ika}+e^{-8ika}$	0	0	0
0	0	0	$e^{2ika}+e^{8ika}$	0	1	0	e^{5ika}
0	0	$e^{-2ika}+e^{-8ika}$	0	1	0	e^{-5ika}	0
0	0	0	0	0	e^{5ika}	0	$1+e^{-6ika}+e^{16ika}$
0	0	0	0	e^{-5ika}	0	$1+e^{6ika}+e^{-16ika}$	0

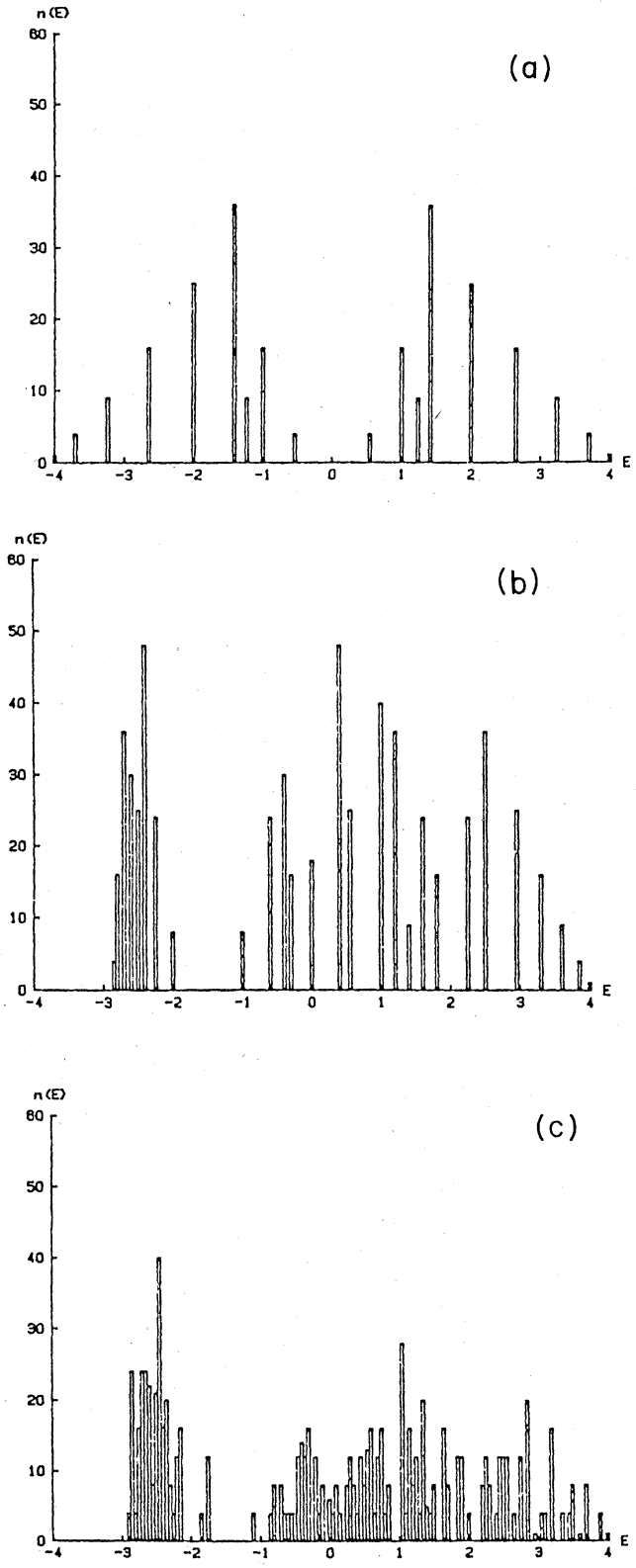

FIG. 19. s-band density of states for (a) polytope 240, (b) polytope {5,3,3}, (c) "polytope 864" [{3,3,5} with a pair of disclinations of the type shown in Fig. 13(b)].

$$k_1=\frac{n\pi}{5a},\quad n=0,1,2,3,4$$
$$k_2=\frac{2m\pi}{10a},\quad m=0,1,\ldots,9\ . \tag{46}$$

The polytope {5,3,3} spectrum is shown in Fig. 19(b). The extreme oddness of the structure (i.e., the large number of odd-membered rings of bonds) manifests itself in the fact that the antibonding limit is far from being attained; a fully antibonding state is highly frustrated on this lattice. Another interesting point is that the spectral region between -2 and -1 is free of eigenvalues. We speculate that this internal gap is a result of the large number of five-membered rings although we cannot give a simple proof. In Appendix B, which contains a discussion of the effect of disclinations on the polytope electronic spectrum, we give an indirect illustration of the effect of ring parity on this spectral region.

V. sp_3 ELECTRONIC STRUCTURE CALCULATION—POLYTOPE 240

In this section we embark on more detailed electronic and optical structure calculations for one of the polytope models described above, polytope 240. There is evidence that this polytope provides a more realistic model of amorphous Si than the other polytopes. For example, it has been shown[7] that unlike {5,3,3} and polytope 3000,[6] polytope 240 has an atomic density which is comparable to both a-Si and to diamond x-Si. In addition, polytope 240 is known to provide a reasonable description of the local order in certain continuous random-network models of tetrahedrally-bonded amorphous semiconductors,[6,29] the Connell-Temkin[9] model in particular. We have previously provided a rationale for the occurrence of polytope-240-like local order by demonstrating that small finite clusters of polytope 240 (on the order of 24 atoms) can have fewer dangling bonds than diamondlike clusters of comparable size, and thus may be energetically favorable on this small scale.[11] The boatlike rings in the polytope-240 structure have a twist-type distortion, but this does not preclude its formation; it can be shown[8] that this twist requires no bond-length and no bond-angle distortions, and thus may occur with little energy cost. In fact, this twisted ring actually occurs in a high pressure crystalline phase of Si, Si III (Ref. 30) [also shown as "BC8" (Ref. 31)]. This crystal may be viewed as a Frank-Kasper[32] phase of Si with ideal polytope-240 structure threaded by a dense network of disclination lines.[17]

For these reasons we have performed a more quantitative study of the electronic and optical properties of polytope 240. While it is known that the s-band models of electronic structure described above give a qualitatively correct description of the valence band of Si or Ge through the Weaire-Thorpe transformation,[28] these models have certain pathologies (e.g., an infinite-mass p band at the valence-band edge) and provide a poor description of the conduction-band structure. Therefore, in this section we reexamine the electronic structure of Si in the polytope-240 structure using a more extensive tight-binding model developed recently by Vogl, Hjalmar-

TABLE V. s-band Hamiltonian for polytope $\{5,3,3\}$.

$2\cos(2k_ya)$	$e^{ik_xa/4}$	$e^{-ik_xa/4}$	0	0	0	0	0	0	0	0	0
$e^{-ik_xa/4}$	0	$2\cos(k_ya)\times e^{ik_xa/2}$	1	0	0	0	0	0	0	0	0
$e^{ik_xa/4}$	$2\cos(k_ya)\times e^{-ik_xa/2}$	0	0	1	0	0	0	0	0	0	0
0	1	0	0	$e^{-ik_xa/2}$	$e^{ik_xa/4}\times e^{ik_ya/2}$	$e^{ik_xa/4}\times e^{-ik_ya/2}$	0	0	0	0	0
0	0	1	$e^{ik_xa/2}$	0	$e^{-ik_xa/4}\times e^{-ik_ya/2}$	$e^{-ik_xa/4}\times e^{ik_ya/2}$	0	0	0	0	0
0	0	0	$e^{-ik_xa/4}\times e^{-ik_ya/2}$	$e^{ik_xa/4}\times e^{ik_ya/2}$	0	0	$e^{-ik_xa/2}\times e^{ik_ya/4}$	$e^{ik_xa/2}\times e^{-ik_ya/4}$	0	0	0
0	0	0	$e^{-ik_xa/4}\times e^{ik_ya/2}$	$e^{ik_xa/4}\times e^{-ik_ya/2}$	0	0	$e^{ik_xa/2}\times e^{ik_ya/4}$	$e^{-ik_xa/2}\times e^{-ik_ya/4}$	0	0	0
0	0	0	0	0	$e^{ik_xa/2}\times e^{-ik_ya/4}$	$e^{-ik_xa/2}\times e^{-ik_ya/4}$	0	$e^{ik_ya/2}$	1	0	0
0	0	0	0	0	$e^{-ik_xa/2}\times e^{ik_ya/4}$	$e^{ik_xa/2}\times e^{ik_ya/4}$	$e^{-ik_ya/2}$	0	0	1	0
0	0	0	0	0	0	0	1	0	0	$2\cos(k_xa)\times e^{-ik_ya/2}$	$e^{ik_ya/4}$
0	0	0	0	0	0	0	0	1	$e^{ik_ya/2}\times 2\cos(k_xa)$	0	$e^{-ik_ya/4}$
0	0	0	0	0	0	0	0	0	$e^{-ik_ya/4}$	$e^{ik_ya/4}$	$2\cos(2k_xa)$

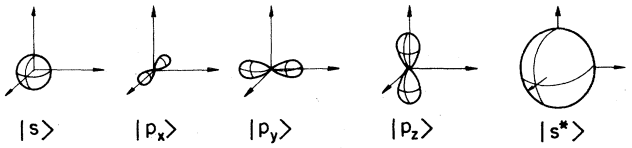

FIG. 20. Tight-binding atomic orbital basis set of Vogl *et al.* (Ref. 33).

son, and Dow[33] which gives a quantitatively correct description of the valence and conduction bands of Si. In this model the normal sp_3 molecular basis set for Si is imagined to be augmented by a fifth orbital, a high energy s orbital (denoted s^*), which is required for a correct description of the free-electron-like conduction band. In this model, matrix elements of the Hamiltonian are assumed to extend only to first neighbors, and the two-center approximation is used.[34] These matrix-element parameters are then fitted so that the known energy bands of diamond Si are reproduced. The quality of the fit is excellent for both the valence and conduction bands, lending support to the physical motivation for adding an extra orbital. The matrix elements which Vogl *et al.* use in the s-p_x-p_y-p_z-s^* orbital basis set (shown schematically in Fig. 20) are listed in Table VI. We have checked the transferability of Vogl's sp_3-s^* model by using these matrix elements in a calculation of the energy-band structure of hexagonal Si, that is, Si in the wurtzite crystal structure. The results are in reasonable agreement (to the 0.5-eV level) with previously published empirical pseudopotential calculations.[31] This result is significant for our polytope calculations because like polytope 240, the wurtzite crystal contains a different dihedral angle ($\phi=0°$) than in the diamond crystal.

In our polytope studies, we have found it more convenient to work in a hybrid orbital basis related to the atomic orbitals through a unitary transformation; these hybrids are shown in Fig. 21. They are given in terms of the atomic orbital basis by the unitary transformation:

$$
\begin{aligned}
|sp_3\rangle_1 &= \tfrac{1}{4}(|s\rangle+|p_x\rangle+|p_y\rangle+|p_z\rangle)\,,\\
|sp_3\rangle_2 &= \tfrac{1}{4}(|s\rangle+|p_x\rangle-|p_y\rangle-|p_z\rangle)\,,\\
|sp_3\rangle_3 &= \tfrac{1}{4}(|s\rangle-|p_x\rangle+|p_y\rangle-|p_z\rangle)\,,\\
|sp_3\rangle_4 &= \tfrac{1}{4}(|s\rangle-|p_x\rangle-|p_y\rangle+|p_z\rangle)\,.
\end{aligned}
\tag{47}
$$

The matrix elements in this basis are

TABLE VI. Atomic orbital matrix elements in sp_3-s^* basis set (in eV).

$E_s=-4.2$	$V_{xy}=4.575$
$E_p=1.715$	$V_{sp}=5.7292$
$V_{ss}=-8.3$	$E_{s^*}=6.685$
$V_{xx}=1.715$	$V_{s^*p}=5.3749$

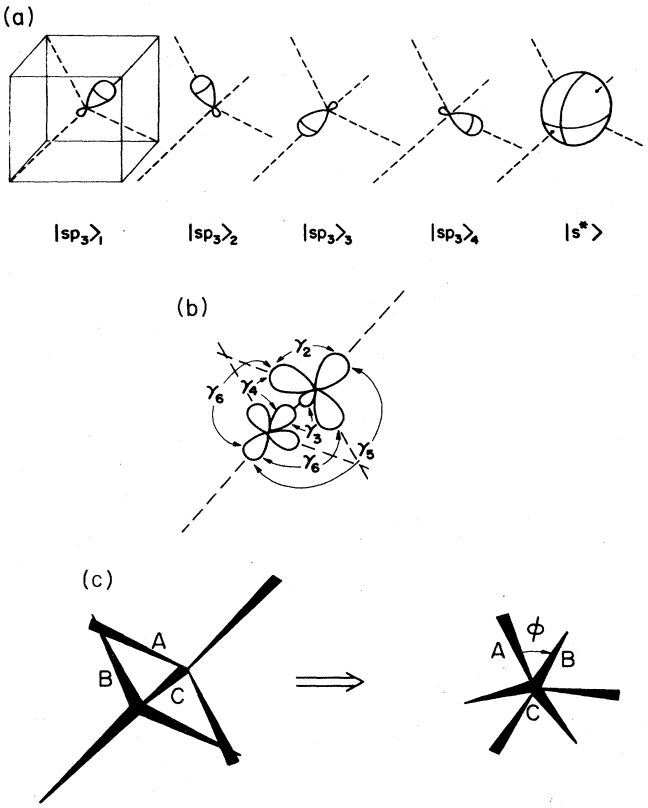

FIG. 21. (a) Hybrid-orbital basis set constructed from linear combinations of the orbitals in Fig. 20. (b) Hybrid-orbital Hamiltonian matrix elements as defined in Eq. (48) of the text. (c) Definition of the dihedral angle ϕ. It is the angle between bonds A and B when viewed along bond C.

$$
\begin{aligned}
\gamma_1 &= \tfrac{1}{4}(E_s+3E_p)\,,\\
\gamma_2 &= \tfrac{1}{4}(E_s-E_p)\,,\\
\gamma_3 &= \tfrac{1}{16}(V_{ss}-3V_{xx}-6V_{xy}-6V_{sp})\,,\\
\gamma_4 &= \tfrac{1}{16}(V_{ss}+V_{xx}+2V_{xy}-2V_{sp})\,,\\
\gamma_5 &= \tfrac{1}{16}(V_{ss}+V_{xx}-2V_{xy}+2V_{sp})\,,\\
\gamma_6 &= \tfrac{1}{16}(V_{ss}-3V_{xx}+2V_{xy}+2V_{sp})\,,\\
\gamma_7 &= E_{s^*}\,,\\
\gamma_8 &= -\tfrac{3}{8}V_{s^*p}\,,\\
\gamma_9 &= \tfrac{1}{8}V_{s^*p}\,.
\end{aligned}
\tag{48}
$$

The values of these hybrid matrix elements as derived from the original parameters are given in Table VII. The hybrid orbitals point along the four tetrahedral bond directions, and as such are easier to define in curved space (recall that the bonds are just defined as geodesics in S^3). As we show below, they also make the construction of a model optical-absorption function more natural. The matrix elements of these basis functions, indicated in Fig. 21,

TABLE VII. Hybrid orbital matrix elements (in eV).

$\gamma_1=0.236$
$\gamma_2=-1.479$
$\gamma_3=-4.704$
$\gamma_4=-0.556$
$\gamma_5=-0.267$
$\gamma_6=0.448$
$\gamma_7=6.685$
$\gamma_8=-2.016$
$\gamma_9=0.672$

still involve only coupling between states on neighboring atoms. However, they depend on the dihedral angle ϕ, which *does* involve the position of more than two atoms (it is, as Figs. 21 shows, the angle between bonds A and B on neighboring atoms as viewed down the common bond C). The dihedral angle is different in polytope 240 than in diamond Si. It may be obtained by projecting the structure locally into Euclidean space, in which the dihedral angle is well defined. (ϕ may also be directly defined in the non-Euclidean space by a parallel transport operation in S^3.) We find the dihedral angle ϕ to be about 37.1°, intermediate between the eclipsed $\phi=0°$ and the staggered $\phi=60°$ configuration. With use of the standard two-center approximation[34,35] the matrix elements γ' for any arbitrary dihedral angle ϕ are given by a simple linear combination of the γ_5 and γ_6 for the eclipsed dihedral angle, as follows:

$$\gamma'=\tfrac{2}{3}(\gamma_5-\gamma_6)\cos\phi+\tfrac{2}{3}\gamma_5+\tfrac{1}{3}\gamma_6 . \tag{49}$$

For the polytope-240 dihedral angle ($\phi\approx 37.1°$) this gives, using the parameter values of Table VII,

$$\gamma'_5=-0.27\text{eV} ,$$
$$\gamma'_6=0.45\text{ eV} . \tag{50}$$

It is these parameters, along with the $\gamma_1-\gamma_4,\gamma_7,\gamma_8$ defined above, which we use in the electronic structure calculation for polytope 240.

As in Sec. III above, we use the order 30 cyclic Abelian subgroup of the polytope-240 group [which corresponds to the screw rotation axis along the channeling direction of Fig. 16(a)] to diagonalize the electronic Hamiltonian. Then, as above, the structure has an eight-atom "unit cell," and the size of the secular matrix is 40, that is, 8 (atoms) times 5 (orbitals). The one-dimensional "wave vector" $\mathbf{k}$ can take on 30-discrete values, since it is simply the label of the 30 one-dimensional irreducible representations of the 30-element cyclic group. We have diagonalized the secular matrix at these allowed $\mathbf{k}$ points, producing the points on the "band structure" of Fig. 22. As a consequence of the finite size of the polytope model, the system has only discrete, "molecular" energy levels rather than having continuous energy bands. Nevertheless, the simple structure of the symmetry label permits a continuous energy-band structure (the lines in Fig. 22) to be constructed in a natural way. As shown in the simpler s-band secular equation in Table IV, the wave vector $\mathbf{k}$ enters only in factors of the form $\exp(2\pi nk/30)$. Thus we may simply diagonalize the secular equation for any arbitrary value of $\mathbf{k}$; this amounts to performing a smooth analytic continuation between the energy points in Fig. 22. While these eigenvalues have no meaning for polytope 240 itself, they could be relevant, for example, in a structure where the channeling structure of Fig. 16(a) extended for a distance larger than ~35 Å, i.e., further than the linear dimensions of the ideal polytope.

Comparison of Fig. 22 with Fig. 18(b) reveals a strong similarity between the s bands of polytope 240 and the lower part of the sp_3-s^* valence bands. This is a simple consequence of the Weaire-Thorpe mapping[25,28] between the s bands and an sp_3 Hamiltonian for which $\gamma_{4-9}=0$ (Ref. 35). However, in the Weaire-Thorpe model, the conduction bands would be a mirror image of the valence bands. In the sp_3-s^* model they are not, which is simply a result of the greater realism of the Vogl *et al.* model. Also, in the Weaire-Thorpe electronic structure the closely-spaced set of bands near the top of the valence bands in Fig. 22 (the "heavy-hole" bands) would all lie on the line $E=0$ and have zero bandwidth, rather than the ~3.5-eV bandwidth in the sp_3-s^* calculation.

The main overall feature of the energy bands of Fig. 22 [and of Fig. 18(b)] is that the bands almost repeat along the K axis with a period of $K=2\pi/3$, a third of the fundamental period $K=2\pi$. The reason for this can be seen in Fig. 16(a). The $\frac{30}{11}$ channel consists of three (110)-like chains; the symmetry operation $\mathbf{T}$, which is reciprocal to K, returns to the same chain every three turns. Thus, the phase of the Bloch function advances by e^{3iKa} from one segment of a chain to the next. Therefore, from the point of view of a single chain, the Brillouin-zone periodicity is given by $3K=2\pi$, as seen in the figures. This periodicity is not exact because of chain-chain coupling.

Other aspects of these energy bands are elucidated by an approximate analogy to the surface energy-band structure of a diamond Si crystal. Imagine the walls of the channel in Fig. 16(a) to be a free surface which has been rolled up on itself. Then the (110) chains running along

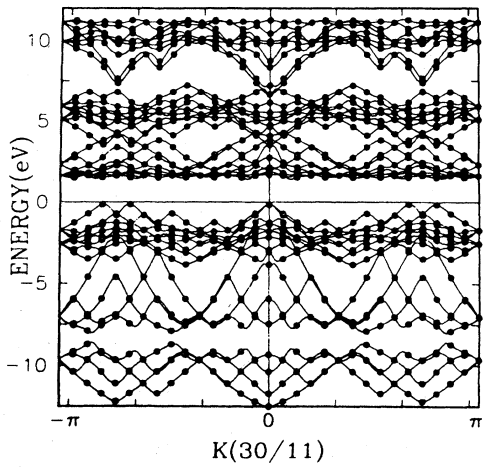

FIG. 22. Energy bands of polytope 240, calculated in the sp_3-s^* basis. The allowed energy eigenvalues of the polytope are shown as solid circles.

this "surface" make it somewhat reminiscent of the unreconstructed (111) surface of a diamond crystal (see Fig. 23) The $\frac{30}{11}$ screw translation **T** in Fig. 16(a) corresponds to the surface lattice translation **T** in Fig. 23. In addition, since the $\frac{30}{11}$ channel contains just three chains, the atoms labeled *A* and *B* in the Si(111) surface are identified with the same atom in the polytope-240 structure. This means that eigenstates of polytope 240 should be identified with the surface energy states of a Si diamond crystal which are periodic upon translation in the surface from atom *A* to atom *B*. This restricts the surface wave vectors of interest to the line shown in Fig. 24. This figure shows the reciprocal space of the Si(111) surface in the repeated zone scheme. The states along the line shown [in a (451) direction when referred to the bulk diamond crystal] have **k** perpendicular to $\mathbf{T}_{AB}$. Thus $\mathbf{k}_{AB}=0$, and the state is periodic in the direction $\mathbf{T}_{AB}$ as required. The $K(\frac{30}{11})$ wave-vector labeling of Fig. 22 can be mapped onto this line in Fig. 24. As this shows, one Brillouin zone of the channeling axis maps extends through three Brillouin zones of the (111) surface. This observation provides and alternate explanation for the occurrence of a quasiperiodicity in the energy bands of Figs. 19 and 22 with three periods inside each Brillouin zone.

This surface analogy also explains why the $\frac{30}{11}$ energy bands have a "filled-in" appearance, that is, with entire regions of the *E* vs *K* plot filled up with bands. These simply correspond to the projected bulk bands in the surface problem.[36] The valence bands have a maximum at $K(\frac{30}{11})=0$; this can be thought of as a simple consequence of the fact that the valence-band maximum in the bulk diamond structure at Γ is projected onto $K(\frac{30}{11})=0$, as indicated in Fig. 24. On the other hand, the bulk conduction-band minimum, which in *x*-Si occurs 0.85 of the way along the Γ—*X* line, does not project onto the $K(\frac{30}{11})$ line in Fig. 24 (see the open circles). This helps to explain why the conduction-band edge for the polytope is quite flat. While these analogies are quite useful for understanding the general form of the energy bands of the polytope, it is important to remember that these comparisons should not be taken too literally. While the *local* bonding geometry of the $\frac{30}{11}$ axis is similar to that on the *x*-Si (111) surface, the *overall* topology is quite different.

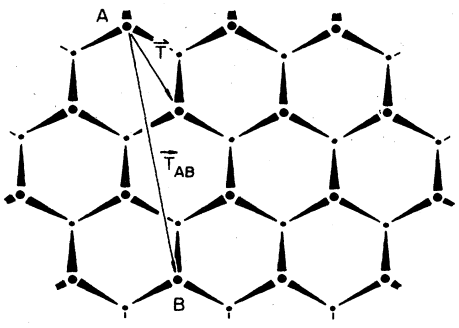

FIG. 23. Schematic unwrapping of the structure in Fig. 16(b) onto a (111) surface. Atoms *A* and *B* are identified as identical in the polytope structure. The translation **T** corresponds to the screw symmetry operation **T** in Fig. 16(a).

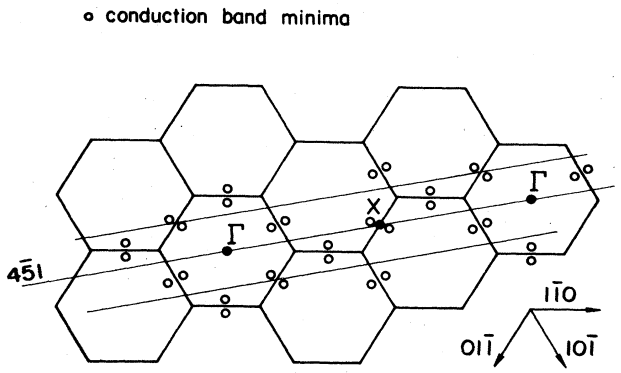

FIG. 24. Surface reciprocal space corresponding to Fig. 23. The $\frac{30}{11}$ reciprocal lattice in Fig. 22 maps onto the 4$\bar{5}$1 line shown. This line passes through the surface Γ point, but it avoids the points which corresponds to the projected bulk conduction-band minimum in Si (open circles).

In no sense should there be an exact correspondence between the two energy-band diagrams, and in fact similar approximate comparisons can be made between the $\frac{30}{11}$ bands and the bands of other Si surfaces, e.g., (110) (Ref. 11).

VI. OPTICAL PROPERTIES

In crystalline solids translational symmetry leads to the vertical selection rule of optical absorption,

$$k_f - k_i = 0 \ . \tag{51}$$

Amorphous solids have no translational symmetry. The normal conclusion from this has been[37] that no selection rules of any kind govern optical absorption: an optical transition is equally likely from *any* valence-band state to *any* conduction-band state. In this section we explore the consequences of the polytope model for optical selection rules. Since the polytope symmetries cannot be exact symmetries of the amorphous solid, no exact selection rules will come out of this model. However, to the extent that the amorphous solid looks like the polytope *locally*, e.g., if a $\frac{30}{11}$ channel with *N* turns occurs in the amorphous solid, then an approximate selection rule will be obtained in terms of the polytope "wave vector" defined above, viz.,

$$| K(\tfrac{30}{11})_f - K(\tfrac{30}{11})_i | \lesssim \pi/N \ . \tag{52}$$

We begin by supposing that the amorphous solid is composed of local regions of polytope which have been flattened out so as to fit into Euclidean space; this is the so called "orange-peel carpet" picture of an amorphous solid[6,38] (see Fig. 25 for a two-dimensional example). In the independent particle approximation, the imaginary part of the dielectric function of this system is given by the usual expression:[15]

$$\epsilon_2(h\nu) = \frac{e^2}{\Omega_0 h^2 \nu^2} \sum_{\mathrm{VB,CB}} \left| \int \Psi^*_{\mathrm{VB}}(\mathbf{r}) p_x \Psi_{\mathrm{CB}}(\mathbf{r}) d^3r \right|^2 , \tag{53}$$

$$= \frac{e^2}{\Omega_0 \nu^2} \sum_{\mathrm{VB,CB}} \left| \int \Psi^*_{\mathrm{VB}}(\mathbf{r}) [x, H] \Psi_{\mathrm{CB}}(\mathbf{r}) d^3r \right|^2 . \tag{54}$$

FIG. 25. Orange-peel carpet picture of the amorphous solid. The equicontours of the optical field are superimposed.

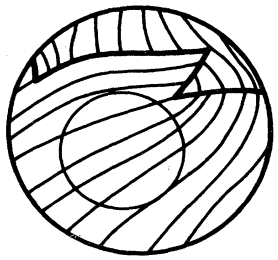

FIG. 26. Orange peel rewrapped back onto curved space. We have carried the contours of the optical field along. Locally they still look like the optical field in flat space (circled region).

Here Ω_0 is the volume per atom in the solid, and the valence-band (VB) and conduction-band (CB) wave functions are normalized to $1/\sqrt{N}$ within one atomic volume, with N being the number of atoms in the solid. H is the Hamiltonian, and ν is the frequency. The polarization is assumed to be in the x direction, shown in the Fig. 25. The equivalue contours of the x operator merely consist of straight lines normal to the $\hat{x}$ direction as shown. Our goal is to construct a sensible idealization of this quantity which is computable directly on the polytope itself. We accomplish this by imagining that we perform the inverse orange-peel mapping, i.e., that we rewrap one of the patches of Fig. 25 back onto a sphere. In addition, we imagine that the equicontours of the optical-absorption operator x are also carried back onto the sphere by this inverse mapping (see Fig. 26). Our approximation for the dielectric functions would then be given by

$$\epsilon_2(h\nu)\approx\left\langle\frac{e^2}{\Omega_0\nu^2}\sum_{\mathrm{VB,CB}}\left|\int\Psi^*_{\mathrm{VB}}(\mathbf{r}_s)[f(\mathbf{r}_S),H^{240}]\Psi_{\mathrm{CB}}(\mathbf{r}_S)d^3r_S\right|^2\right\rangle_{\{f(\mathbf{r}_S)\}}. \tag{55}$$

Here $f(\mathbf{r}_S)$ is the optical operator x of Eq. (54) after mapping back into curved space. It is a vector field obtainable from the gradient of the function shown in Fig. 26. The angular brackets indicate an average over all possible mapped fields. Note that while for illustrative purposes we show and describe our approximations to ϵ_2 in 2D, the necessary generalization to 3D is very straightforward. In this formulation the strain disorder resulting in a change of the local orientation of the polytope structure with respect to the electric field direction is included, but the disorder in the electronic eigenstates is ignored, i.e., the perfect polytope Hamiltonian H^{240} is used.

We now discuss the details of the evaluation of Eq. (55). In second-quantized notation the valence- (or conduction-) band wave functions can be written

$$\Psi_{\mathrm{VB}}=\sum_i c^i_{\mathrm{VB}}\,|\,i\,\rangle \tag{56}$$

where $|\,i\,\rangle$ represents the tight-binding state centered at site i, and c^i_{VB} are the eigenstate coefficients as computed in Sec. V. The matrix element inside Eq. (55) can then be written

$$M=\sum_{i,j}(c^i_{\mathrm{VB}})^*\langle i\,|\,(fH^{240}-H^{240}f)\,|\,j\,\rangle c^j_{\mathrm{CB}}. \tag{57}$$

Here the asterisk denotes complex conjugation and f is the optical operator defined above. We now insert a complete set of states $|\,k\,\rangle$:

$$M=\sum_{i,j,k}(c^i_{\mathrm{VB}})^*(\langle i\,|\,f\,|\,k\,\rangle\langle k\,|\,H\,|\,j\,\rangle - \langle i\,|\,H\,|\,k\,\rangle\langle k\,|\,f\,|\,j\,\rangle)c^j_{\mathrm{CB}}. \tag{58}$$

We now use the standard approximation within tight-binding theory for the position matrix element:[15]

$$\langle i\,|\,f\,|\,j\,\rangle\approx\delta_{ij}f(\mathbf{r}_{Si}). \tag{59}$$

The matrix element can finally be written

$$M=\sum_{i,j}(c^i_{\mathrm{VB}})^*H^{240}_{ij}(f(\mathbf{r}_{Si})-f(\mathbf{r}_{Sj}))c^j_{\mathrm{CB}}. \tag{60}$$

Therefore, our expression for ϵ_2 becomes

$$\epsilon_2\approx\left\langle\frac{e^2}{\Omega_0\nu^2}\sum_{\mathrm{VB,CB}}\left|\sum_{i,j}(c^i_{\mathrm{VB}})^*H^{240}_{ij}(f(\mathbf{r}_{Si})-f(\mathbf{r}_{Sj}))c^j_{\mathrm{CB}}\right|^2\right\rangle_{\{f(\mathbf{r}_s)\}}. \tag{61}$$

We must now discuss our approximation to the mapped optical field $f(\mathbf{r}_S)$. In Fig. 26 we see that while the typical field $f(\mathbf{r}_S)$ is strongly disordered in regions near the cut lines of the orange-peel map, there are large regions of the sphere in which it will have a very regular structure (see the circled region of Fig. 26). Within these regions $f(\mathbf{r}_S)$ may be approximated by an idealized field whose equivalue contours are shown in Fig. 27(a), consisting of simply the "latitude lines" of the sphere. The equation for the field f in this latitude approximation is

$$f(\mathbf{r}_s)=x_i \ , \tag{62}$$

where x_i is one of the four Cartesian coordinates of the Euclidean space in which the polytope is embedded. This approximation to f is very appealing because the optical-absorption expression obtained by using it,

$$\epsilon_{2ij}(h\nu)=\frac{e^2}{\Omega_0\nu^2}\left[\int \Psi^*_{\mathrm{VB}}(\mathbf{r}_S)[x_i,H^{240}]\Psi_{\mathrm{CB}}(\mathbf{r}_S)d^3r_S\right]^* \times\left[\int \Psi^*_{\mathrm{VB}}(\mathbf{r}_S)[x_j,H^{240}]\Psi_{\mathrm{CB}}(\mathbf{r}_S)d^3r_S\right], \tag{63}$$

is formally a symmetric second-rank tensor. It can be shown that within the symmetry group of polytope 240 ($O'\times Y'/\mathbb{Z}_2$), there is only one distinct symmetric second-rank tensor which transforms as the identity representation;[39] i.e., $\epsilon_{2ij}=\epsilon_2\delta_{ij}$. This means that polytope 240 is optically isotropic, so that the direction of the optical field does not matter. Therefore, in the average $\langle\ \rangle_{\{f(\mathbf{r}_S)\}}$ of Eq. (61), which represents an averaging over both the shape and orientation of $f(\mathbf{r}_S)$, the average over orientation need not be done. We will make the further approximation of discarding the average over the shape of the field, and we will compute the optical absorption for one particular idealized mapped field:

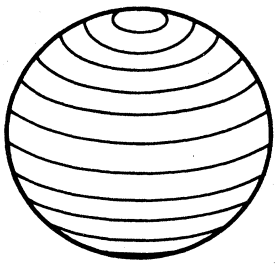

FIG. 27. An idealized optical field corresponding to the latitude lines of the sphere.

$$\epsilon_2(h\nu)=\frac{e^2}{\Omega_0\nu^2}\sum_{\mathrm{VB,CB}}\left|\sum_{i,j}(c^i_{\mathrm{VB}})^*H^{240}_{ij}(f^{\mathrm{ideal}}(\mathbf{r}_{Si})-f^{\mathrm{ideal}}(\mathbf{r}_{Sj}))c^j_{\mathrm{CB}}\right|^2 . \tag{64}$$

While we could use Eq. (62) for f^{ideal}, we have actually used a more complicated form. The field of Eq. (62) has the defect of any Mercator projection on a sphere, namely that it causes a severe elongation of lengths near the poles. The form which we use more nearly preserves length on the entire sphere:

$$f^{\mathrm{ideal}}(\mathbf{r}_{Si})-f^{\mathrm{ideal}}(\mathbf{r}_{Sj})=(R^2-\langle w^2\rangle-\langle x^2\rangle)^{1/2}[\tan^{-1}(z_i/y_i)-\tan^{-1}(z_j/y_j)] \ . \tag{65}$$

Here

$$\langle w^2\rangle\equiv\tfrac{1}{2}(w_i^2+w_j^2) \ , \tag{66}$$

and R is the radius of the three-sphere. Equation (65) defines the form of f^{ideal} which we use in our calculation of optical absorption, Eq. (64). This choice of f^{ideal} corresponds more nearly to using "longitude lines" rather than "latitude lines" as in Eq. (62). Equation (65) has the disadvantage that ϵ_2 is no longer exactly a symmetric second-rank tensor; it is therefore not precisely rotationally invariant. However, since the f^{ideal}'s of Eqs. (65) and (62) are very closely related, we expect the dependence of ϵ_2 on the orientation of the optical field to be insignificant. In addition, there is a symmetry argument which shows that the optical absorption remains unchanged when f^{ideal} is oriented along any of the equivalent $\frac{30}{11}$ directions. It is easy to show that any atom in polytope 240 belongs to 12 distinct $\frac{30}{11}$ channels, which run off in the directions shown in Fig. 28. It can be seen from this figure that it is impossible to orient f^{ideal} more than about 20° away from a $\frac{30}{11}$ direction; therefore, the optical absorption cannot vary much as a function of direction.

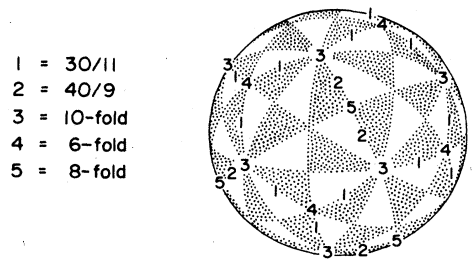

FIG. 28. Symmetry axes to which a given atom in polytope 240 belongs. The directions from the center of the sphere to the points indicated on its surface give the directions of the various screw axes. The directions are shown with reference to an icosahedral pattern. There are 12 $\frac{30}{11}$ channels for a given atom, more than any other type. There are also four sixfold axes (going out along directions corresponding to the vertices of a cube), six tenfold axes (passing through the vertices of an icosahedron), three eightfold axes (in octahedral directions), and six $\frac{40}{9}$ axes.

We can show the existence of vertical selection rules by studying the symmetry properties of optical absorption in Eq. (64). Consider a symmetry translation of the $\frac{30}{11}$ screw type, i.e., the operation **T** in Fig. 16(a). The Hamiltonian is of course invariant with respect to this operation. The Δf of Eq. (65) also remains invariant under this operation [recall that f is measured locally along the $\hat{x}$ direction of Fig. 16(a)]. Therefore the operator $H\,\Delta f$ of Eq. (64) is invariant under **T** and belongs to the identity representation of the $\frac{30}{11}$ group. According to the normal rules of group theory,[40] this means that nonzero contributions to Eq. (64) only occur when the eigenvectors $c_{\rm VB}$ and $c_{\rm CB}$ belong to the same representation of the group. In our language above this means that they must have the same $K(\frac{30}{11})$. Therefore, *optical transitions are vertical.* Under the assumptions which we have made, the polytope structure has optical selection rules which are as strong as in crystalline solids. Of course, many of these assumptions cause this result to be only approximate for the real amorphous solid. For example, our optical field [Eq. (65)] lacks the strong disorder along the cut lines of Fig. 26, which are an inevitable consequence of the orange-peel mapping. However, we know that for certain special kinds of disorder (e.g., disclinations), the selection rule is preserved (see Appendix B).

Nevertheless, we believe that the typical effect of these cuts, spaced by a dimension κ^{-1} (see Fig. 25), is like that of placing a piece of the polytope inside a box of length κ^{-1} (the curvature of the polytope). From the uncertainly principle, this confinement should lead to a wave vector spreading on the order of π/κ^{-1} [see Eq. (52)]. Since the typical size of κ^{-1} is expected to be several lattice constants,[6] this should lead to a breakdown of the vertical selection rules such that transitions over $\sim$20—30% of the Brillouin zone are allowed. So, the vertical selection rule should only be relaxed, not destroyed. There is a potentially more serious assumption we have made, namely that the Hamiltonian is simply that of polytope 240. We thus neglect all bond-length and bond-angle disorder, any effects due to odd-membered rings of bonds, any states resulting from dangling bonds, and any impurity states. (However, see Appendix B.) Still, a preliminary examination of continuous random-network simulations[41,8] seems to suggest that the disordered network can have large regions with small bond length and angle disorder, with no dangling bonds, and with polytope-240-like bonding topology. The use of H^{240} is justifiable under these circumstances.

Figure 29 presents the results of our model ϵ_2 calculation using Eq. (64). Since the ensemble averaging of Eq. (55) has not been performed and since polytope 240 contains a finite number of atoms, the result of evaluating Eq. (64) is actually a discrete line spectrum. We have turned this into a continuous spectrum by giving it a small Gaussian broadening. Its overall magnitude has been adjusted to that the optical sum rule[42] is satisfied. This curve has the overall features which one would expect for any semiconductor: a low absorption region at low energy followed by a fairly sharp rise at the fundamental gap. The wiggles in the spectrum above threshold are a remnant of the underlying line spectrum and should not be taken seriously.

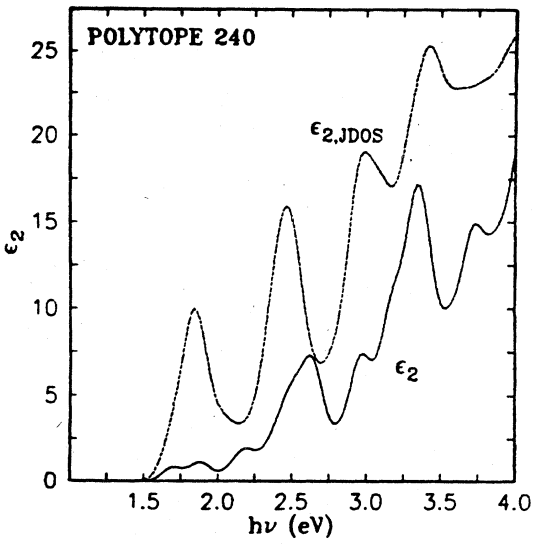

FIG. 29. Solid line: The imaginary part of the dielectric function ϵ_2 as a function of energy, calculated using polytope-240 selection rules [Eq. (64)]. Dashed line: ϵ_2 calculated by ignoring optical selection rules. This quantity is simply proportional to the joint density of states as shown in Eq. (67). Note that ϵ_2 is smaller than $\epsilon_{2,\rm JDOS}$ near the band edge; the selection rules suppress optical absorption in this energy range. The structure in these curves is an artifact of the finiteness of the polytope model.

We wish to compare this optical absorption with one computed by more standard arguments. The usual method of performing this calculation[37] in amorphous solids to assume that there are no selection rules of any kind, and that a transition is equally likely from any valence-band state to any conduction-band state. Under this assumption ϵ_2 is given as a convolution of the conduction- and valence-band densities of states:

$$\epsilon_{2,\rm JDOS}=\frac{1}{R(h\nu)^2}\sum_i N_{\rm VB}(E_i)N_{\rm CB}(E_i+h\nu)\ . \qquad (67)$$

Here R is a normalization factor which has been chosen to satisfy the sum rule, and $N_{\rm VB}$ and $N_{\rm CB}$ are the valence- and conduction-band densities of states. Equation (67) has been used as a justification of the usual Tauc plot for optical absorption in amorphous semiconductors;[43] the fundamental assumption which goes into Eq. (67), namely that the optical matrix element is constant in energy, has been explored experimentally with varying results.[44] We cannot address as subtle a question as the energy variation of the optical matrix element; however, we will show that the inclusion of polytope-like selection rules can have a real effect on the calculated ϵ_2.

To do this, we have first computed the conduction- and valence-band densities of states $N(E)$ from our $\frac{30}{11}$ band structure. The results have appeared earlier[5,14] and are shown in Fig. 30. This density of states has the normal features of any model for $N(E)$ of Si; a three-peaked valence band separated from the conduction band by a $\sim$1-eV gap. This is consistent with a great deal of previ-

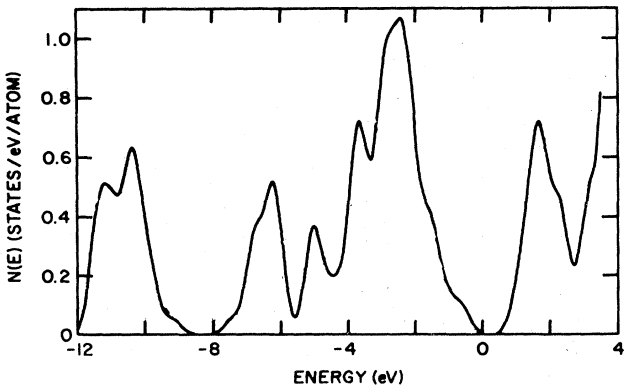

FIG. 30. sp_3-s^* density of states for polytope 240. This quantity is used in Eq. (67).

ous work[45,46,2,47,48] which shows that $N(E)$ is almost entirely a function of only the local tetrahedral bonding topology of Si. With this $N(E)$ we have performed the convolution indicated in Eq. (67), and the resulting spectrum is shown as the dashed line in Fig. 29. As for ϵ_2 calculated the other way, the peaks and valleys are artifacts of the finiteness of the underlying structural model. Setting this aside, however, it is clear that there is a distinct difference between these two curves, with the ϵ_2 computed without selection rules lying generally higher than the other over the entire energy range shown. This is quite a natural result for Si, which is an indirect band-gap material in its crystalline form, meaning that the absorption of the crystal near the fundamental gap is very weak because of selection-rule effects. We speculate that the small value of the ϵ_2 curve in Fig. 29 computed with full selection rules may be manifestation of a sort of band indirectness. Even though Fig. 22 does not show an indirect gap in the conventional sense, it appears that some selection rules in addition to the vertical K selection rule keep the optical matrix element between states near the band edges weak. These additional selection rules could arise, for example, from other screw symmetries of polytope 240 (see Sec. III F), and it is possible that the energy bands appropriate to one of the other symmetry axes should show a real indirectness. These questions await further investigation.

VII. DISCUSSION AND CONCLUSIONS

The polytope model is just one element of a large and rapidly growing effort to understand the structure and properties of noncrystalline materials. We believe that the concept of using lattice structures of higher dimensionality[49] will be a powerful unifying concept in this area.

In the area of close-packed disordered solids, a Gaussian model based on a polytope order parameter has already provided a reliable theory[5] for the glassy structure factor, that most fundamental of structural probes. With use of this order parameter, it is predicted that the real disordered solid can be thought of as a dense tangled array of disclination lines in a polytope medium;[17] this point of view is supported by the occurrence of the Frank-Kasper crystalline phases,[32,51–53] which can be described as materials with an ordered array of such disclination lines. A renormalization group has been constructed[38] for such a close-packed order parameter which shows that a sensible continuum theory[54] does exist for these materials.

No such order parameter yet exists for the covalently-bonded amorphous solids, but there is substantial reason to believe that it can be constructed. Many approaches are possible, but one which appears promising would take the orientational part of the order parameter to be octahedral rather than icosahedral as in the close-packed materials. A tentative study of the "BC8" high-pressure crystalline polytope of Si (Ref. 30) lends support to this order parameter; "BC8" seems to be the analog of a Frank-Kasper phase for covalent materials, with an ordered array of 120° disclination lines. There are many questions which this order parameter must answer to make these ideas into a complete theory. For example, the polytope-240 description implies that the tetrahedrally-bonded amorphous solid should have a local handedness; if experimental investigations prove this to be true, it must be incorporated into a more systematic theory. A complete classification of defect lines must also be considered. One hint in this direction is provided by the result of Rivier[55] that odd-membered rings must occur in strings; one would strongly suspect that these strings are disclination lines within a correct theory. However, it also seems likely from looking at "BC8" and at the Connell-Temkin[9] random-network model (which contain only even-membered rings) that a complete classification of disclinations include "strings" of even-membered rings as well. In searching for a complete description of the covalent solids it is possible that useful analogies with the better-understood close-packed solids can be made; the relationship between these materials *via* "decoration" might result in an association between the defect lines of the covalent material and an associated close-packed solid.[26]

On other important issues we must at the present admit a total lack of understanding. A close link must exist between the occurrence and structure of defect lines and the electronic and transport properties of the amorphous material. Despite some tentative suggestions elsewhere[17] and in the present paper (Appendix B), no such link has been established. In particular, it is not clear whether the symmetry quantum numbers discussed in the present work will be preserved in a rigorous sense in a theory containing defects. On another front, an entirely new class of materials have been recently discovered[56] which have *long-ranged* icosahedral orientational order (like polytope {3,3,5}), but quasiperiodic translational order. It is not clear if polytope-type models have any role in describing these fascinating new solids.[57,58]

To summarize, we have further extended the polytope model in its application to tetrahedrally-bonded amorphous semiconductors. The central motivation for introducing the polytope structure as a model for local order is that certain types of propagated short-range order are not compatible with long-range translational order, but are compatible with a polytope lattice. Therefore, polytope

symmetries should provide approximate quantum numbers labeling eigenstates in the disordered solid. We have reviewed the symmetry groups and representations of several of the polytopes, and have demonstrated the way in which eigenstates may be systematically indexed with these symmetry groups within a simple tight-binding model. Polytope 240 is the best candidate for local order in amorphous Si; therefore, we have performed a detailed calculation of its electronic structure using a more realistic multiorbital tight-binding model. We can show a strong resemblance between the results obtained and a conventional band structure for crystalline Si. We show that an approximate vertical selection rule pertains to optical absorption in this model, and we speculate that this may contribute to the depressed optical absorption near the fundamental band edge in hydrogenated amorphous Si.

ACKNOWLEDGMENTS

It is a pleasure to thank J. P. Gaspard, D. R. Nelson, and M. Widom for several enlightening discussions. Also, thanks to J. P. Sethna for a critical reading of this manuscript. Thanks to F. S. Khan for help with Fig. 8. This work was partially supported by the National Science Foundation through the Materials Science Center at Cornell University.

APPENDIX A: QUATERNIONS

We briefly recall the main properties of quaternions. For a more complete description, see Refs. 18 and 19. We follow the presentation of Ref. 19. Quaternions can be defined as ordered pairs of complex numbers with the following rules for addition and multiplication:

$$(s,t)+(u,v)=(s+u,\ t+v)\ ,$$
$$(s,t)(u,v)=(su-t\bar{v},\ sv+t\bar{u})\ ; \tag{A1}$$

$s,u,t,v\in\mathbb{C}$ and $\bar{u}$ is the complex conjugate of u. A quaternion a can equivalently be written

$$a=u+vj,\quad u,v\in\mathbb{C}\ . \tag{A2}$$

The new entity j combines with i (the pure imaginary) according to

$$jij=i,\quad iji=j\ . \tag{A3}$$

One can then define the conjugate $\tilde{a}$ of a quaternion $a=u+vj$:

$$\tilde{a}=\bar{u}-vj\ . \tag{A4}$$

Also the norm N_a is

$$N_a=a\tilde{a}=\tilde{a}a=u\bar{u}+v\bar{v}>0\ . \tag{A5}$$

Another interesting way of writing the quaternion a is

$$a=a_0+a_1i+a_2j+a_3k,\quad a_0,a_1,a_2,a_3\in\mathbb{R}\ , \tag{A6}$$

with $i^2=j^2=k^2=ijk=-1$. Yet another way in which a can be written is as a scalar part S_a and a vector part V_a:

$$a=S_a+V_a,\quad S_a=a_0,\quad V_a=a_1i+a_2j+a_3k\ , \tag{A7}$$

with the relations

$$S_a=\tfrac{1}{2}(a+\tilde{a}),\quad V_a=\tfrac{1}{2}(a-\tilde{a})\ . \tag{A8}$$

A quaternion is said to be real if $V_a=0$ and pure imaginary if $S_a=0$. Finally, a unit quaternion (of unit norm) can be written

$$a=\cos\alpha+y\sin\alpha\ , \tag{A9}$$

or

$$a=\exp(\alpha y)\ , \tag{A10}$$

where y is a pure imaginary quaternion. Remember that quaternion multiplication is not commutative so

$$\exp(\alpha y)\exp(\beta z)=\exp(\alpha y+\beta z) \tag{A11}$$

only if $y=z$.

APPENDIX B: TOPOLOGICAL DEFECTS AND ELECTRONIC SPECTRA

We begin with a simple two-dimensional polytope, the cube (see Fig. 6). A disclination of angle $\pi/2$ along the fourfold "vertical" axis transforms the cube into a pentagonal prism (Fig. 31). This structure is topologically related to the infinite ladder on the right-hand side of Fig. 6 by identifying every fifth (rather than every fourth) site along the ladder. The eigenvalues are given by diagonalizing the same expression as the for the cube (Table II), but the "allowed" $\mathbf{k}$ values are now

$$\mathbf{k}=\frac{2\pi n}{5a},\quad n=0,1,2,3,4\ . \tag{B1}$$

In this simple example we see that the defect-induced modification of the spectrum is described most simply when the disclination axis and the symmetry axis coincide. This remains true in the polytope case.

Figure 13(b) shows the local effect of a $2\pi/5$ disclination line threading a fivefold symmetry axis in $\{5,3,3\}$. This fivefold axis along with another one constitute the pair of spherical torus axes described in Fig. 8. If $2\pi/5$ disclinations are introduced along both of these axes, a 864-vertex structure with lower curvature than $\{5,3,3\}$ is produced. The electronic spectrum of this polytope is obtained by the diagonalization of the same 12×12 matrix of Table V, but the "allowed" $\mathbf{k}$ values are

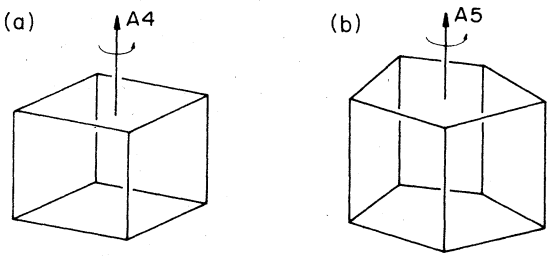

FIG. 31. Insertion of a disclination into a cube.

$$k_1=\frac{n\pi}{6a},\quad n=0,1,2,3,4,5\ ,$$
$$k_2=\frac{m\pi}{12a},\quad m=0,\ldots,11\ . \tag{B2}$$

The s-band density of states of "polytope 864" is shown in Fig. 19(c). Compared with $\{5,3,3\}$, the lower band edge has been pushed (very slightly) toward the antibonding limit at -4. This is a consequence of the introduction of some even-membered (6) rings along the disclination axes. The presence of these six-membered rings correlates with the appearance of eigenstates between -2 and -1 in the figure. This is why we attribute the gap in the $\{5,3,3\}$ spectrum to the extreme "oddness" of the structure [see discussion below Eq. (46)].

The s-band density of states of "polytope 864" bears a strong resemblance to the density of states of $\{5,3,3\}$. At first sight one could say that the former could be derived from the latter by some broadening process. The advantage of the spherical torus method is that it brings to light the exact relationship of that broadening to the topological defect.

[1]See, e.g., *The Physics of Hydrogenated Amorphous Silicon,* edited by J. D. Joannopoulos and G. Lucovsky (Springer, Berlin, 1984); *Amorphous Semiconductors,* edited by M. H. Brodsky (Springer, Berlin, 1979).

[2]D. C. Allan and J. D. Joannopoulos, *The Physics of Hydrogenated Amorphous Silicon II,* edited by J. D. Joannopoulos and G. Lucovsky (Springer, Berlin, 1984), p. 5.

[3]M. Kléman and J. F. Sadoc, J. Phys. (Paris) Lett. **40**, L569 (1979).

[4]J. F. Sadoc, J. Non-Cryst. Solids **44**, 1 (1981).

[5]M. H. Brodsky and D. P. DiVincenzo, J. Non-Cryst. Solids **59&60**, 101 (1983).

[6]J. F. Sadoc and R. Mosseri, Philos Mag. B **45**, 467 (1982).

[7]J. F. Sadoc and R. Mosseri, J. Phys. Colloq. **42**, C4-189 (1981).

[8]M. H. Brodsky and D. P. DiVincenzo, in Proceedings of the Eleventh Internation Conference on Amorphous and Liquid Semiconductors, Rome, 1985 (unpublished).

[9]G. A. N. Connell and R. J. Temkin, Phys. Rev. B **9**, 5323 (1974).

[10]D. E. Polk and D. S. Boudreaux, Phys. Rev. Lett. **31**, 92 (1973).

[11]M. H. Brodsky, D. P. DiVincenzo, R. Mosseri, and J. F. Sadoc, in *Proceedings of the Seventeenth International Conference on the Physics of Semiconductors,* edited by J. D. Chadi and W. A. Harrison (Springer, Berlin, 1985), p. 803.

[12]H. S. M. Coxeter, *Regular Polytopes* (Methuen, London, 1948).

[13]M. H. Brodsky and D. P. DiVincenzo, Physica **117&118B**, 971 (1983).

[14]D. P. DiVincenzo, R. Mosseri, M. H. Brodsky, and J. F. Sadoc, Phys. Rev. B **29**, 5934 (1984).

[15]W. A. Harrison, *Electronic Structure and the Properties of Solids* (Freeman, San Francisco, 1980), p. 98.

[16]M. H. Brodsky, R. S. Title, K. Weiser, and G. D. Petit, Phys. Rev. B **1**, 2632 (1970).

[17]David R. Nelson and Michael Widom, Nucl. Phys. **B240 [FS12]**, 113 (1984).

[18]Patrick DuVal, *Homographies, Quaternions and Rotations* (Clarendon, Oxford, 1964).

[19]H. S. M. Coxeter, *Regular Complex Polytopes* (Cambridge University Press, London, 1974).

[20]E. Goursat, Ann. Sci. Ec. Norm. Super. **6**, 9 (1889).

[21]N. P. Warner, Proc. R. Soc. London, Ser. A **383**, 379 (1982).

[22]J. D. Bernal, Proc. R. Soc. London, Ser. A **280**, 299 (1964).

[23]H. S. M. Coxeter, *Introduction to Geometry* (Wiley, New York, 1969), p. 412.

[24]G. de B. Robinson, Proc. Camb. Phil. Soc. **27**, 37 (1931); H. S. M. Coxeter, Philos. Trans. R. Soc. London, Ser. A **229**, 346 (1930). We are indebted to H. S. M. Coxeter for bringing this work to our attention.

[25]M. Widom, Phys. Rev. B **31**, 6456 (1985).

[26]D. R. Nelson and M. Widom (private communication).

[27]J. Friedel, J. Phys. (Paris) **39**, 651 (1978).

[28]D. Weaire and M. F. Thorpe, Phys. Rev. B **4**, 2508 (1971).

[29]S. Sachdev and D. R. Nelson (private communication).

[30]R. H. Wentorf and J. S. Kasper, Science **139**, 338 (1963).

[31]J. D. Joannopoulos and Marvin L. Cohen, Solid State Phys. **31**, 71 (1976).

[32]F. C. Frank and J. S. Kasper, Acta. Crystallogr. **11**, 184 (1958); **12**, 483 (1959).

[33]P. Vogl, H. P. Hjalmarson, and J. D. Dow, J. Phys. Chem. Solids **44**, 365 (1983).

[34]J. C. Slater and G. F. Koster, Phys. Rev. **94**, 1498 (1954).

[35]Fumiko Yonezawa and Morrel H. Cohen, in *Fundamental Physics of Amorphous Semiconductors,* edited by F. Yonezawa (Springer, Berlin, 1981), p. 119

[36]Actually, these bands bear an even greater resemblance to a slab model, in which the infinite bulk is represented by a finite number of layers of atoms.

[37]G. A. N. Connell, in *Amorphous Semiconductors,* edited by M. H. Brodsky (Springer, Berlin, 1979), p. 73.

[38]James P. Sethna, Phys. Rev. B **31**, 6278 (1985).

[39]G. Ya. Lyubarskii, *The Application of Group Theory to Physics* (Pergamon, New York, 1960), p. 75.

[40]Michael Tinkham, *Group Theory and Quantum Mechanics* (McGraw-Hill, New York, 1964).

[41]F. Wooten, K. Winer, and D. Weaire, in *Proceedings of the Seventeenth International Conference on the Physics of Semiconductors,* edited by J. D. Chadi and W. A Harrison (Springer, Berlin, 1985); Phys. Rev. Lett. **54**, 1392 (1985).

[42]F. Wooten, *Optical Properties of Solids* (Academic, New York, 1972).

[43]J. Tauc, *Amorphous and Liquid Semiconductors* (Plenum, London, 1974).

[44]W. B. Jackson, S.-J. Oh, C. C. Tsai, S. M. Kelso, and J. W. Allen, in *Proceedings of the Seventeenth International Conference on the Physics of Semiconductors,* edited by J. D. Chadi and W. A. Harrison (Springer, Berlin, 1985).

[45]D. P. DiVincenzo, J. Bernholc, and M. H. Brodsky, Phys. Rev. B **28**, 3246 (1983).

[46]D. C. Allan and J. D. Joannopoulos, Phys. Rev. Lett. **44**, 43 (1980).

[47]D. C. Allan, J. D. Joannopoulos, and W. B. Pollard, Phys. Rev. B **25**, 1065 (1982); **26**, 3475 (1982).

[48]E. N. Economou and D. A. Papaconstantopoulos, Phys. Rev. B **23**, 2042 (1981).

[49]See, e.g., V. Elser (unpublished); M. Duneau and A. Katz,

Phys. Rev. Lett. **54**, 2688 (1985).
[50]Subir Sachdev and David R. Nelson, Phys. Rev. Lett. **53**, 1947 (1984).
[51]D. R. Nelson, Phys. Rev. B **28**, 5515 (1983).
[52]J. F. Sadoc, J. Phys. (Paris) Lett. **44**, L707 (1983).
[53]D. R. Nelson, Phys. Rev. Lett. **50**, 982 (1983).
[54]J. P. Sethna, Phys. Rev. Lett. **50**, 2198 (1983).
[55]For example, N. Rivier, in *Proceedings of the 1982 Taniguchi Symposium on the Nature of Topological Disorder* (Springer, Berlin, 1983).
[56]D. Schechtman, I. Blech, D. Gratias, and J. W. Cahn, Phys. Rev. Lett. **53**, 1951 (1984).
[57]Dov Levine and Paul Joseph Steinhardt, Phys. Rev. Lett. **53**, 2477 (1984).
[58]R. Mosseri and J. F. Sadoc, J. Phys. (Paris) Lett. **45**, L827 (1984).